

Atomically Modulating Competing Exchange Interactions in Centrosymmetric Skyrmion Hosts GdRu_2X_2 ($\text{X} = \text{Si}, \text{Ge}$)

Dasuni N. Rathnaweera,¹ Xudong Huai,¹ K. Ramesh Kumar,¹ Michał J. Winiarski,² Tomasz Klimczuk,² and Thao T. Tran^{1,*}

¹Department of Chemistry, Clemson University, Clemson, South Carolina, 29634, United States

²Faculty of Applied Physics and Mathematics and Advanced Materials Center, Gdansk University of Technology, ul. Narutowicza 11/12, 80-233 Gdansk, Poland

KEYWORDS: Magnetic skyrmion, magnetic anisotropy, RKKY exchange interactions, magnetoentropy

ABSTRACT: Magnetic skyrmions are topologically protected spin states enabling high-density, low-power spin electronics. Despite growing efforts to find new skyrmion host systems, the microscopic mechanisms leading to skyrmion phase transitions at specific temperatures and magnetic fields remain elusive. Here, we systematically study the isostructural centrosymmetric magnets— GdRu_2X_2 ($\text{X} = \text{Si}$ and Ge)—and the role of $\text{X-}p$ orbitals in modifying magnetic exchange interactions. GdRu_2Ge_2 single crystals, synthesized by arc melting, exhibit two high-entropy pockets associated with skyrmion phases at $0.9 \text{ T} \leq \mu_0 H \leq 1.2 \text{ T}$ and $1.3 \text{ T} \leq \mu_0 H \leq 1.7 \text{ T}$, $2 \text{ K} \leq T \leq 30 \text{ K}$ —more accessible condition at lower fields and higher temperatures than that in the Si counterpart. Entropy estimations from heat capacity measurements align with magnetization data, and transport studies confirm a topological Hall effect, highlighting the system’s nontrivial spin textures and Berry curvature. Compared to GdRu_2Si_2 , electronic structure and exchange interaction evaluations reveal the more extended $\text{Ge-}4p$ orbitals enhance competing exchange interactions in GdRu_2Ge_2 , thereby manifesting the rich skyrmion behavior. This work demonstrates how modifying exchange interactions at the atomic level enables the tunability of topologically nontrivial electronic states while advancing our understanding of skyrmion formation mechanisms for future spintronics.

INTRODUCTION

Understanding the chemistry and physics underlying the evolution of topologically distinct spin textures—magnetic skyrmions—and their behaviors is essential for advancing future information and energy technologies.^[1] Magnetic skyrmions, displaying a unique, dynamic quasiparticle character with a size ranging from a few to ~ 100 nm, can enable high-density, low-power spintronics and logic functions.^[2] The topological protection ensures skyrmions retain their unique spin properties, even in the presence of defects and disorders, which are inevitable in real materials. The formation of magnetic skyrmions is mainly driven by two fundamental mechanisms based on crystal symmetries. In noncentrosymmetric magnets, the asymmetric Dzyaloshinskii-Moriya interaction, facilitated by large spin-orbit coupling, can stabilize skyrmion formation.^[3] In centrosymmetric magnetic metals, the long-range Ruderman-Kittel-Kasuya-Yosida (RKKY) exchange interaction $J(r) \sim \sin(2k_F r) / r^3$, where k_F is the Fermi wavevector of conduction electrons and r is the distance between the magnetic moments, assisted by magnetic frustration, facilitates skyrmion evolution.^[2c, 4] Enhanced competing ferromagnetic (FM) and antiferromagnetic (AFM) interactions at a similar energy scale promote the emergence of skyrmions.

Small-sized skyrmions in centrosymmetric magnetic metals often display higher topological charge density compared to those in noncentrosymmetric counterparts. This feature is a key for enhancing the topological Hall effect—a physical phenomenon with significant implications for advanced spintronic technologies.^{[4c], [2c, 5]} Centrosymmetric skyrmion hosts are limited to a few metals adopting cubic, hexagonal, and tetragonal crystal lattices with Gd^{3+} and Eu^{2+} ($S = 7/2$, $L = 0$) spins, such as Gd_2PdSi_3 , $Gd_3Ru_4Al_{12}$, $EuAl_4$, and $EuGa_2Al_2$.^[4d, 6] Recent theoretical studies on centrosymmetric tetragonal lattices suggested several factors influencing skyrmion formation, such as frustrated exchange interactions, easy-axis anisotropy, bond-dependent anisotropy, and positive biquadratic interactions.^[7] While these studies presented tremendous progress in skyrmion materials research, a picture of how competing exchange interactions can be modified at the atomic and molecular levels remains unclear. This is a daunting task due to the intricate nature of skyrmion hosts and phase transitions to skyrmions at a given field and temperature.

$GdRu_2Si_2$ was found to display a skyrmion pocket at $2\text{ T} \leq \mu_0 H \leq 2.5\text{ T}$, $2\text{ K} \leq T \leq 20\text{ K}$, with the smallest diameter of 1.9 nm among the known skyrmion materials.^[8] It has been demonstrated that indirect RKKY interactions stabilize equivalent magnetic modulation vectors, resulting in a square skyrmion lattice in the Si material.^[8-9] $GdRu_2Ge_2$ —an isostructural sibling—has recently been realized to feature the successive formation of two

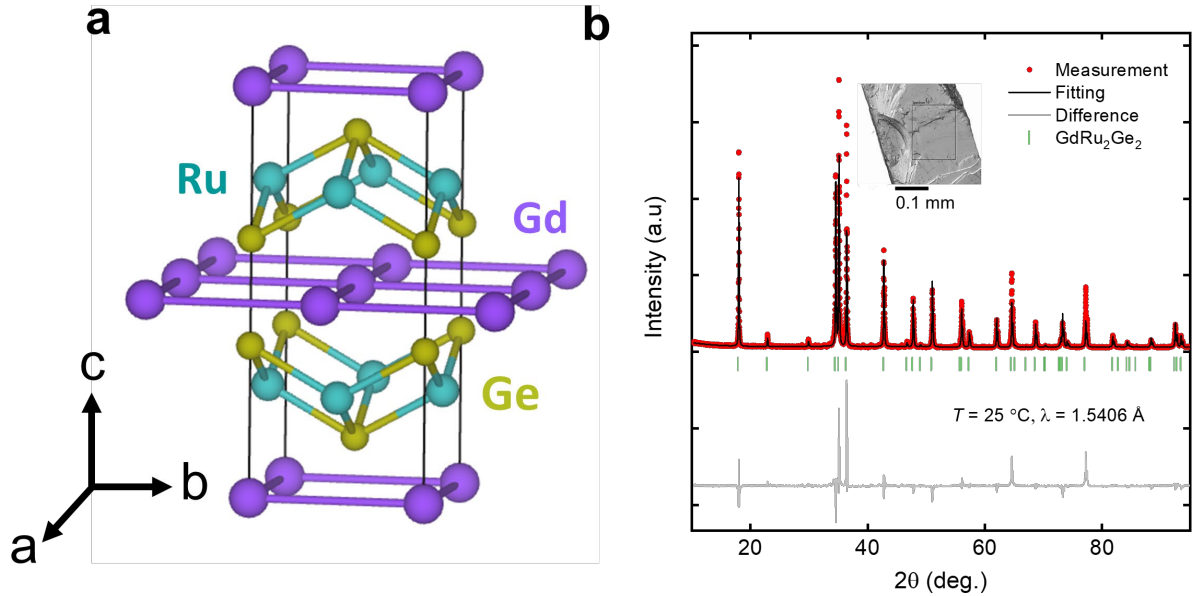


Figure 1. (a) Crystal structure of GdRu_2Ge_2 with the Gd^{3+} square lattice, (b) Rietveld refinement of powder X-ray diffraction data showing phase purity of GdRu_2Ge_2 and inset figure showing scanning electron microscopic image of GdRu_2Ge_2 .

skyrmion phases at $0.9 \text{ T} \leq \mu_0 H \leq 1.2 \text{ T}$ and $1.3 \text{ T} \leq \mu_0 H \leq 1.5 \text{ T}$, $2 \text{ K} \leq T \leq 30 \text{ K}$.^{[10],[11]} Studies showed that this rich topological behavior is governed by the presence of competing RKKY exchange interactions at inequivalent wavevectors.^[11] While GdRu_2X_2 ($\text{X} = \text{Si}$ and Ge) presents an exciting system for tuning skyrmion phase transitions, the underlying reasons that lead to different critical field and temperature conditions at which the skyrmion phase transitions take place are not understood.

To address this, our work focused on understanding the role of the $\text{X-}p$ orbitals in modifying the Gd-Gd magnetic exchange interactions in GdRu_2X_2 and whether and/or how this interplay contributes to the critical temperature and field of the phase transition to skyrmions. We synthesized GdRu_2Ge_2 crystals and characterized their structural, magnetic, thermodynamic, and transport properties. We then supplemented the experimental results with density functional theory (DFT) calculations for spin-polarized band structure, density of states, and magnetic exchange interactions. The integrated approach enables us to gain some insights into the impact of $\text{Si-}3p/\text{Ge-}4p$ orbitals on the Gd-Gd magnetic exchange interactions while linking this interplay to the skyrmion phase transitions in GdRu_2X_2 .

RESULTS AND DISCUSSION

Our single crystal X-ray diffraction measurements confirmed that GdRu₂Ge₂ adopts the ThCr₂Si₂-type structure—a centrosymmetric tetragonal space group *I4/mmm* (**Figure 1**, **Table S1-2**). The structure of GdRu₂Ge₂ consists of Gd square nets connected to [Ru₂Ge₂] layers. The Gd—Gd, Ru—Ge, and Gd—Ge bond distances are 4.23, 2.42, and 3.26 Å, respectively (**Table S3**). Our powder Rietveld refinement agreed well with the structure determined from the single crystal data (**Figure 1b**). Scanning Electron Microscopy (SEM) coupled with Energy Dispersive X-ray (EDS) (**Figure S1**) analysis proved the chemical composition of GdRu₂Ge₂. We observed the formation of two skyrmion phases in GdRu₂Ge₂ in the magnetoentropic mapping at $2 \text{ K} \leq T \leq 30 \text{ K}$, $0.9 \text{ T} \leq \mu_0 H \leq 1.2 \text{ T}$ and $1.3 \text{ T} \leq \mu_0 H \leq 1.7 \text{ T}$ (**Figure 2**), consistent with the work reported by Yoshimochi et al.^[11] For neutron scattering, and resonant X-ray scattering of the material, the reader is invited to visit the

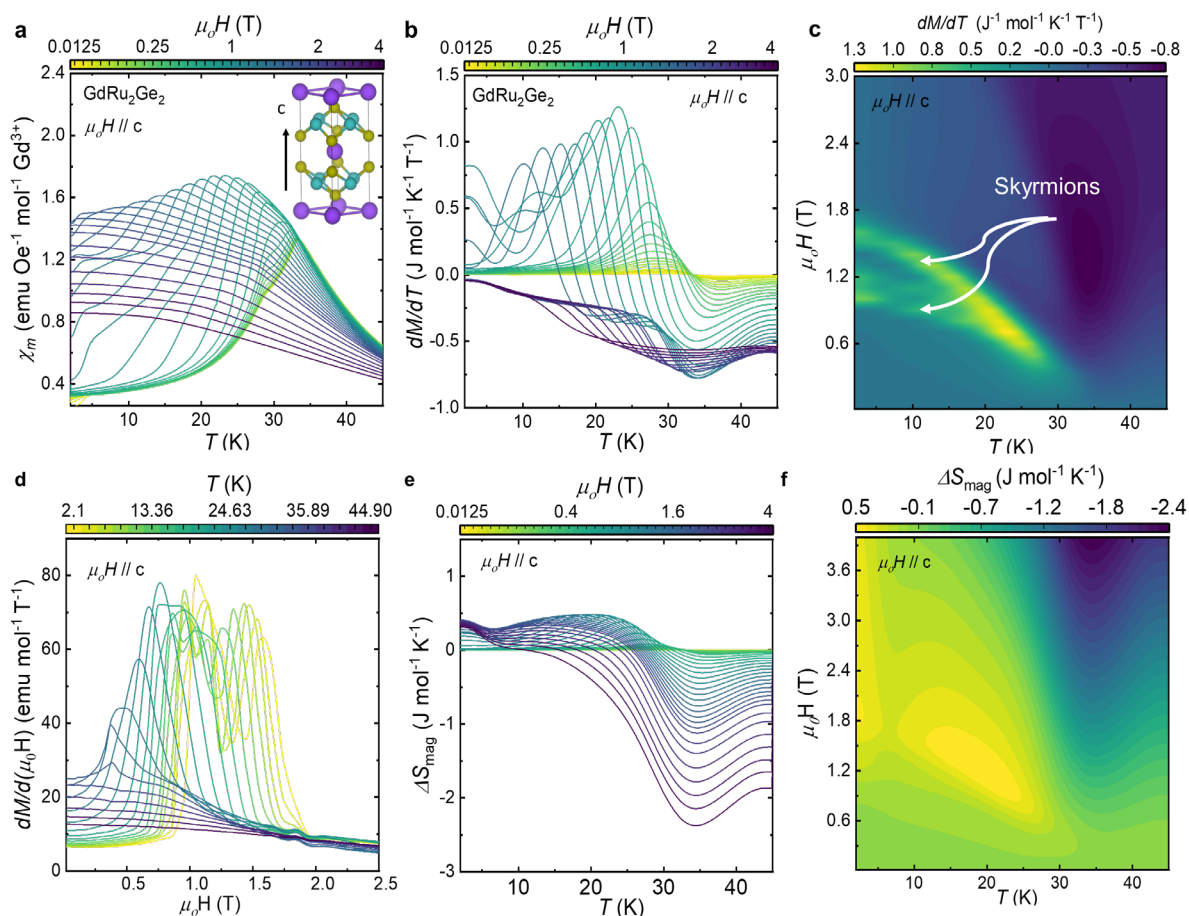


Figure 2. (a) $\chi(T)$ at different magnetic fields $\mu_0 H \parallel c$, (b) First derivative of magnetization with respect to temperature, dM/dT for $\mu_0 H \parallel c$, (c) A map of $dM/dT = dS/dT$ indicating first order transitions, for $\mu_0 H \parallel c$, (d) First derivative of magnetization with respect to the magnetic field dM/dH curve $\mu_0 H \parallel c$, (e) Isothermal magnetic entropy at each different magnetic field obtained by the integral of dM/dT with respect to the magnetic field $\mu_0 H \parallel c$, and (f) A map of $\Delta S_M(T, H)$ of GdRu₂Ge₂.

reference.^[11] Here, we provide a complementary understanding of the thermomagnetic and transport properties of GdRu₂Ge₂ and *how* the Gd—Gd competing exchange interactions in GdRu₂X₂ influence the phase transition conditions at which topological spin textures form.

The emergence of skyrmions typically corresponds to a positive entropy change.^{[12],[13],[14]} The isothermal entropy change upon magnetization $\Delta S_{mag}(H,T)$ can be obtained from the Maxwell relation (Eq. 1),

$$\left(\frac{dS}{dH}\right)_T = \left(\frac{dM}{dT}\right)_H \quad (1)$$

where S is the total entropy, H is the magnetic field, M is the magnetization, and T is the temperature.

Figure 2 depicts how the magnetization of GdRu₂Ge₂ evolves as a function of temperature under a series of applied fields at $\mu_0 H \parallel c$ (**Figure 2a-f**) and $\mu_0 H \perp c$ (**Figure S2**). The magnetic behavior of GdRu₂Ge₂ is orientation-dependent, confirming the magnetic anisotropy in the system as seen in previous studies.^[15] A similar anisotropic behavior was observed in other skyrmion hosts with competing interactions between Gd-Gd spins.^{[16],[17]} At $\mu_0 H \parallel c$, a rich magnetic behavior of GdRu₂Ge₂ is clearly observed in the first derivative of magnetization with respect to temperature dM/dT curves and the magnetoentropic $\Delta S_{mag}(H, T)$ map (**Figure 2a-f**). Anomalies in the dM/dT curves (**Figure 2b**) occur at the critical fields consistent with those identified in the dM/dH curves (**Figure 2d**), confirming the skyrmion phase transitions. The $dM/dT = dS/dH$ and $\Delta S_{mag}(H,T)$ maps of GdRu₂Ge₂ can be constructed from the relation (Eq. 2)

$$\Delta S_{mag}(H, T) = \int_0^H \left(\frac{dM}{dT}\right)_{H'} dH' \quad (2)$$

In the dM/dT map at $\mu_0 H \parallel c$ (**Figure 2c**), green-yellow ridges at $2 \text{ K} \leq T \leq 30 \text{ K}$ and $0.9 \text{ T} \leq \mu_0 H \leq 1.2 \text{ T}$ and $1.3 \text{ T} \leq \mu_0 H \leq 1.7 \text{ T}$ denote the regions of two skyrmion phases. **Figure 2e-f** shows the $\Delta S_{mag}(H,T)$ map highlighting the regions of positive entropy change of approximately $0.5 \text{ J mol}^{-1} \text{ K}^{-1}$. These high entropy pockets correspond to the skyrmion formation—an entropy-driven phase transition. A positive entropy change associated with the evolution of skyrmions sets this state of matter apart from other topologically trivial states, such as helical and conical phases. At $\mu_0 H \perp c$, the magnetoentropic features associated with the skyrmion phase transitions are observed (**Figure S2**), but not as pronounced as those at $\mu_0 H \parallel c$. This divergence confirms the magnetic anisotropy of GdRu₂Ge₂.

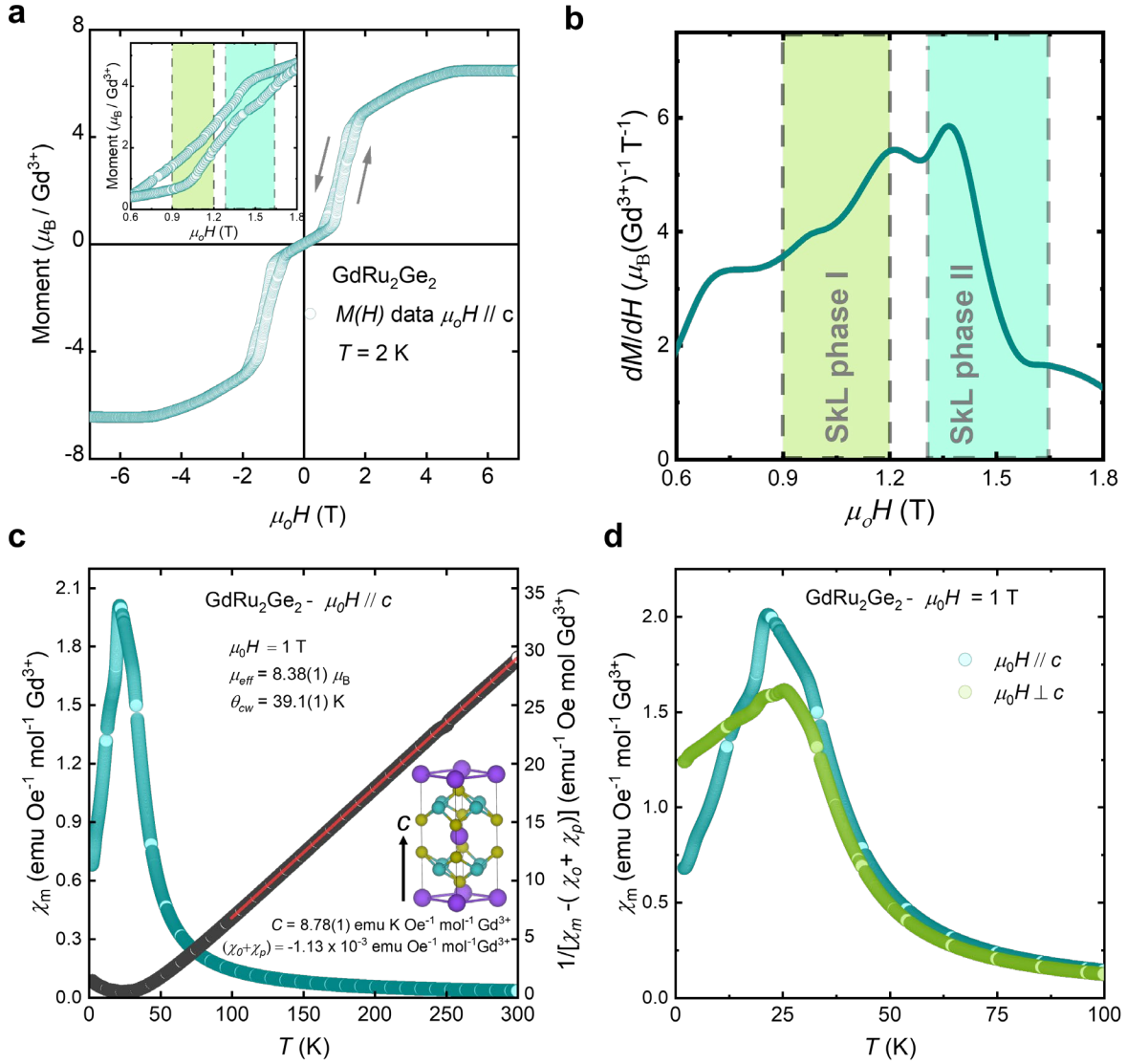


Figure 3. (a) Field dependence of the magnetization measured at $T = 2$ K. (b) First derivative of magnetization with respect to the magnetic field, dM/dH vs. $\mu_0 H$, (c) Temperature-dependent magnetic susceptibility under constant magnetic field $\mu_0 H = 1$ T (teal) and Curie-Weiss analysis (black), and (d) Comparison of temperature-dependent magnetic susceptibilities at $\mu_0 H \perp c$ and $\mu_0 H \parallel c$

The critical fields at which the two skyrmion phases form were identified in the $M(H)$ and the dM/dH curves (**Figure 3a-b**), in good agreement with the results reported by Yoshimochi et al.^[11] The $M(H)$ curves at $T = 2$ K reveal skyrmion and metamagnetic phase transitions before approaching the saturated moment of the FM state ($\sim 7 \mu_B/\text{Gd}^{3+}$) at $\mu_0 H \geq 4.5$ T. This result also highlights that the skyrmion phases are present all the way from the critical temperature $T = 30$ K down to $T = 2$ K. It is worth noting that the emergence of skyrmions in GdRu₂Ge₂ occurs at higher temperature and lower field ($2 \text{ K} \leq T \leq 30 \text{ K}$, $0.9 \text{ T} \leq$

$\mu_0H \leq 1.2$ T and 1.3 T $\leq \mu_0H \leq 1.7$ T) than that in GdRu₂Si₂ (2 K $\leq T \leq 20$ K, 2 T $\leq \mu_0H \leq 2.5$ T).^[8-9]

To understand the thermodynamic properties of the skyrmion host GdRu₂Ge₂, we performed heat capacity measurements at 2 K $\leq T \leq 300$ K, $\mu_0H = 0, 1.2,$ and 1.7 T on a crystal at $\mu_0H \parallel c$ (**Figure 4a**) and polycrystalline sample (**Figure S4**). The difference between these two data sets proves the orientation dependence and magnetic anisotropy in the material. At $\mu_0H = 0$ T, two anomalies at $T_N = 32$ K and $T_1 = 28$ K and a hump at $T_2 = 10$ K are observed (**Figure 4a-b**), consistent with previous works.^[15, 18] The Neel temperature of GdRu₂Ge₂ is also confirmed by its magnetic susceptibility data. The peak at T_1 could be attributed to spin re-orientation to a long-range modulated magnetic state. The hump at around $T_2 \sim 0.3T_N$ can be associated with a Schottky-like anomaly as $k_B T$ approaches the energy splitting between the two lowest-lying states. The peak at T_0 signifies the transition to the skyrmion phases at $\mu_0H = 1.2$ T, in concert with the critical fields identified from the magnetoentropic mapping and dM/dH .

To better understand field-induced metamagnetic phase transitions associated with the skyrmion formation, we analyzed the heat capacity data in more detail. In solids, the lattice vibrations are categorized as acoustic (Debye) and optical (Einstein) modes based on the phase relations of atomic displacement with respect to the propagation direction. Acoustics modes are in phase vibrations where the atoms oscillate collectively, like compressive sound waves, with low frequency, whereas the optical modes are vibrations of atoms or molecules about their mean position typically have a higher frequency. In the absence of low-lying traverse optical (rattling) and dispersionless (single frequency) Einstein modes, the heat capacity expression can be written as:

$$C_p(T) = \gamma T + [9s_D R \left(\frac{T}{\theta_D}\right)^3 \int_0^{\theta_D/T} \frac{x^4}{(e^x - 1)(1 - e^{-x})} dx] \quad (3)$$

where γ is the Sommerfeld coefficient related to electronic contribution to the heat capacity, θ_D is the Debye temperature associated with maximum or cutoff frequency for lattice vibrations, s_D refers to the total number of atoms in the unit cell, and R is the universal gas

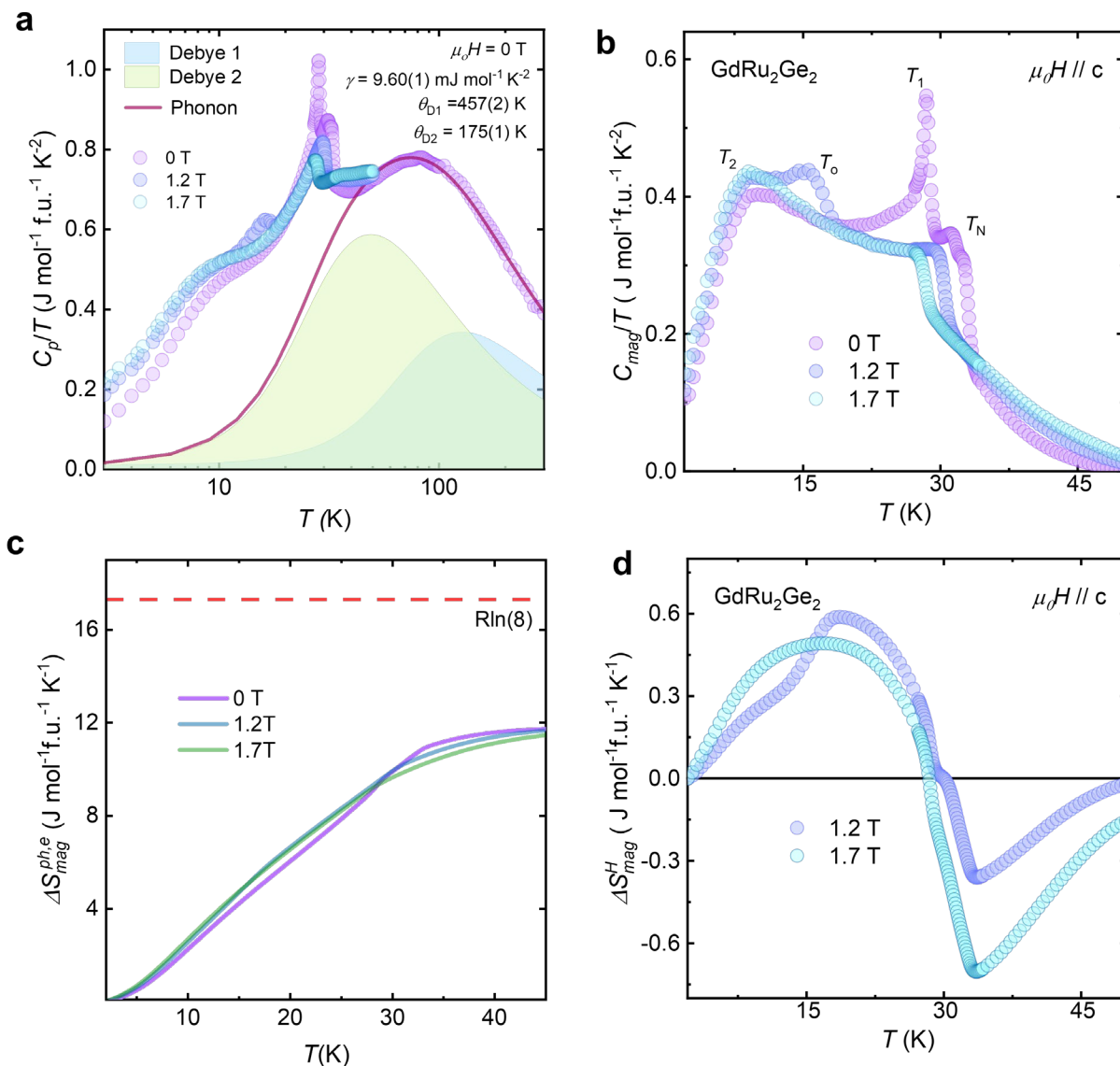


Figure 4. (a) Molar heat capacity over temperature (C_p/T) vs. temperature at different fields. The dark-red line shows the calculated phonons using the two-Debye model for molar heat capacity at $\mu_0 H = 0$ T. (b) Magnetic contribution to the molar heat capacity over temperature (C_{mag}/T) vs. temperature at different fields, (c) Magnetic entropy change w.r.t phonon and electronic contribution, $\Delta S_{\text{mag}}^{\text{ph},e}$, and (d) Magnetic entropy change w.r.t field, ΔS_{mag}^H . The expected value for $R \ln(8)$ is indicated in dashed-red line.

constant. We observed no characteristic T_{\max} peak in the C_p / T^3 vs. $\log(T)$ plot, validating the absence of Einstein (optic) modes (**Figure S5**). We attempted to estimate the low-temperature γ value and β value using the C_p/T vs T^2 linear fitting ($C_p = \gamma T + \beta T^3$), but we observed a linear region at $2 \text{ K} \leq T \leq 5 \text{ K}$ due to the low-lying Schottky anomaly (T_2) associated with Gd^{3+} magnetic ion ground state splitting at $5 \text{ K} \leq T \leq 12 \text{ K}$. Such a narrow range fit may not faithfully reflect the γ and β values and any fitting will underestimate those values. Therefore, we followed the below-mentioned method to estimate the electronic and phonon (lattice vibrations) contributions to heat capacity. At high temperatures, the heat capacity saturates to $120 \text{ J mol}^{-1} \text{ K}^{-1}$, indicating the high temperature limiting value corresponding to 5 atoms satisfied according to the Dulong Petit law ($3nR = 124.71 \text{ J mol}^{-1} \text{ K}^{-1}$). Using the following model, we have chosen a temperature range $50 \text{ K} \leq T \leq 300 \text{ K}$ to fit the heat capacity. The chosen model includes two Debye (acoustic) modes and electronic contribution (Eq. 4-5).

$$\frac{C_p}{T} = \frac{C_{Debye(1)}}{T} + \frac{C_{Debye(2)}}{T} + \gamma \quad (4)$$

$$C_{Debye} = 9Rs_D \left(\frac{T}{\theta_D}\right)^3 D\left(\frac{\theta_D}{T}\right) \quad (5)$$

where s_D is the number of oscillators per formula unit and is generally connected to the total number of atoms in the unit cell. The two Debye functions are warranted to account for low-temperature deviation from quadratic frequency variation of the phonon density of states. Initially, we fixed the γ value based on the estimate from the density of states through the band structure calculation ($\eta(\mathcal{E}_F) = 2.5 \text{ states/eV}$, and $\gamma = 5.9 \text{ mJ mol}^{-1} \text{ K}^{-1}$). During the fitting process, we allowed only the two Debye temperatures to vary and attempted several pairings of s_{D1} and s_{D2} values by keeping the total number of oscillators to 5. We found that the model having $s_{D1} = 3$ and $s_{D2} = 2$ explains the experimental heat capacity data well. Once the phonon contribution to the heat capacity was well-fitted, the γ value was allowed to vary, and the fitting value is shown in **Figure 4a**. We then simulated the electronic and phonon contributions to the heat capacity up to $T = 2 \text{ K}$ using the estimated θ_{D1} , θ_{D2} , and γ values. The electronic contribution γ is $9.60(1) \text{ mJ mol}^{-1} \text{ K}^{-2}$, which is in the same order of magnitude as other magnetic metals.^[19] The increased γ , compared to the theoretical value from the band structure calculation, can stem from a number of possible electron interactions, such as electron-electron, electron-phonon, electron magnon, and spin fluctuations. The magnetic contribution to the heat capacity was estimated at $2 \text{ K} \leq T \leq 50 \text{ K}$ by subtracting the simulated heat capacity. The temperature dependence of C_{mag} is shown in **Figure 4b**. Anomalies in heat capacity data represent the bulk nature of any phase transitions; however, both temperature-driven and entropy-driven transitions show a positive peak in heat capacity measurement. To determine whether the heat capacity peak associated with the skyrmion phase (T_0) corresponds to positive magnetoentropy, we estimated $\Delta S_{\text{mag}}^{ph,e}$ as a function of temperature for all fields using Equation 6.

$$\Delta S_{mag}^{ph,e} = \int_0^T \frac{C_{mag}}{T} dT \quad (6)$$

The subscript denotes the magnetic contribution to the heat capacity, while the superscript indicates the estimation of magnetic entropy relative to the electronic and phonon contributions to the heat capacity. The maximum entropy recovered at $T = 50$ K is ~ 12 J mol⁻¹ f.u.⁻¹ K⁻¹, which is slightly lower than expected for Gd³⁺ local moment ions (**Figure 4c**). A plausible reason for the underestimation of the entropy recovery can be attributed to the presence of a Schottky-type hump, as we mentioned previously. However, our goal here is to make a qualitative analysis of the peak shape corresponding to the skyrmion pocket and not to quantify the isothermal entropy change. We used $\Delta S_{mag}(0, T)$ as a reference to estimate $\Delta S_{mag}^H = \Delta S(H, T) - \Delta S(0, T)$. The magnetic entropy estimated shows a positive peak at $T = 20$ K and a negative peak at $T = 33$ K corresponding to the origin of the skyrmion pocket and AFM ordering, respectively (**Figure 4d**). We illustrated that positive entropy mapping from heat capacity analysis complements insights into skyrmions evolution gained from magnetization measurements while contrasting the phase transitions to topologically distinct skyrmions and other topologically trivial magnetic states. Even though magnetization measurement is more sensitive than heat capacity, heat capacity probes the bulk nature of phase transitions. This combined knowledge highlights that the skyrmion formation in GdRu₂Ge₂ is a lattice phenomenon with periodic modulation, not an isolated pocket or a bubble randomly forming in the lattice, agreeing well with the reported literature.^[11]

To investigate the evidence for the topological features of GdRu₂Ge₂, charge transport properties were measured under magnetic fields down to $T = 2$ K (**Figure 5**). The zero-field temperature dependence of resistance exhibits a typical linear behavior at $50 \leq T \leq 300$ K, as expected for a metallic sample. At $T < 33$ K, we observed a rapid decrease in resistivity, indicating the suppression of spin-disorder scattering, which is expected in all magnetically ordered systems. The resistivity at $T = 2$ K was measured to be $2 \mu\Omega\text{-cm}$, and the residual resistivity ratio (RRR) was found to be ~ 17 . This relatively large RRR value confirms the high quality of the sample. The temperature dependence of ρ_{xx} for several applied fields is shown in **Figure 5a**. The field is applied perpendicular to the current direction. As the field increases, the magnetic ordering temperature decreases. When the field is increased to 2 T, the magnetic ordering becomes smeared out. In applied fields, we would typically expect a decrease in magnetic ordering temperature for a conventional AFM and smearing out of magnetic ordering for an FM system.^[20] Since we observed both the temperature reduction and smearing of the magnetic transitions in response to the applied field for GdRu₂Ge₂, this indicates the presence of competing magnetic interactions. The magnetoresistance (*MR*) is defined as:

$$MR = \frac{R(H) - R(0)}{R(0)} \% \quad (7)$$

where $R(H)$ and $R(0)$ are resistance values at an applied field μ_0H and zero field, respectively.

We observed a large negative MR with a peak-like behavior centered around the magnetic transition (**Figure S6**). The low-temperature positive MR arises from the dominance of the Lorentz contribution. This is owing to the reduction in the spin-wave-related MR upon the magnetic saturation. Apart from the conventional negative MR expected for magnetic metals, we did not observe any signatures of topological features in the MR , as carrier scattering along the longitudinal direction is often insensitive to nontrivial band topology or scalar spin chirality.

To understand these effects, we carried out Hall resistivity (ρ_{xy}) measurements. **Figure 5b** shows the temperature variation of ρ_{xy} at $2 \text{ K} \leq T \leq 50 \text{ K}$ and different applied fields. We observed negative ρ_{xy} in the entire temperature and field range, indicating that the majority of charge carriers are holes. However, the high-field ρ_{xy} data exhibit a nonlinear behavior, which could indicate a multiband effect.

The ρ_{xy} vs. T plot (**Figure 5b**) shows a negative hump-like feature near the magnetic transition at lower fields $\mu_0H = 0.5, 1$ and 1.2 T , and a positive hump at higher fields $\mu_0H = 1.5$ and 2 T . This behavior suggests subtle variations in the electronic structure where charge carriers passing through the magnetic spin swirls (skyrmions) could experience an emergent field, known as the Berry curvature.

In general, the total Hall resistivity ρ_{xy} can be expressed as:

$$\rho_{xy} = \rho_{xy}^{NHE} + \rho_{xy}^{AHE} + \rho_{xy}^{THE} \quad (8)$$

where the first term corresponds to the normal (or ordinary) Hall effect (NHE), which arises due to the Lorentz force and typically varies linearly with the applied magnetic field. The second term represents the anomalous Hall effect (AHE), which originates from anomalous scattering mechanisms in magnetically ordered materials. This contribution is influenced by side-jump and/or skew scattering of charge carriers due to magnetization. The third term accounts for the topological Hall effect (THE), which appears only in materials with nontrivial electronic states exhibiting Berry curvature in momentum space or in materials hosting skyrmions or magnetic spin vortices in the real-space lattice^[21]. The topological hall contribution can be estimated by carefully removing the ρ_{xy}^{NHE} and ρ_{xy}^{AHE} .

$$\Delta\rho_{xy} \text{ or } \rho_{xy}^{THE} = \rho_{xy} - (\rho_{xy}^{NHE} + \rho_{xy}^{AHE}) \quad (9)$$

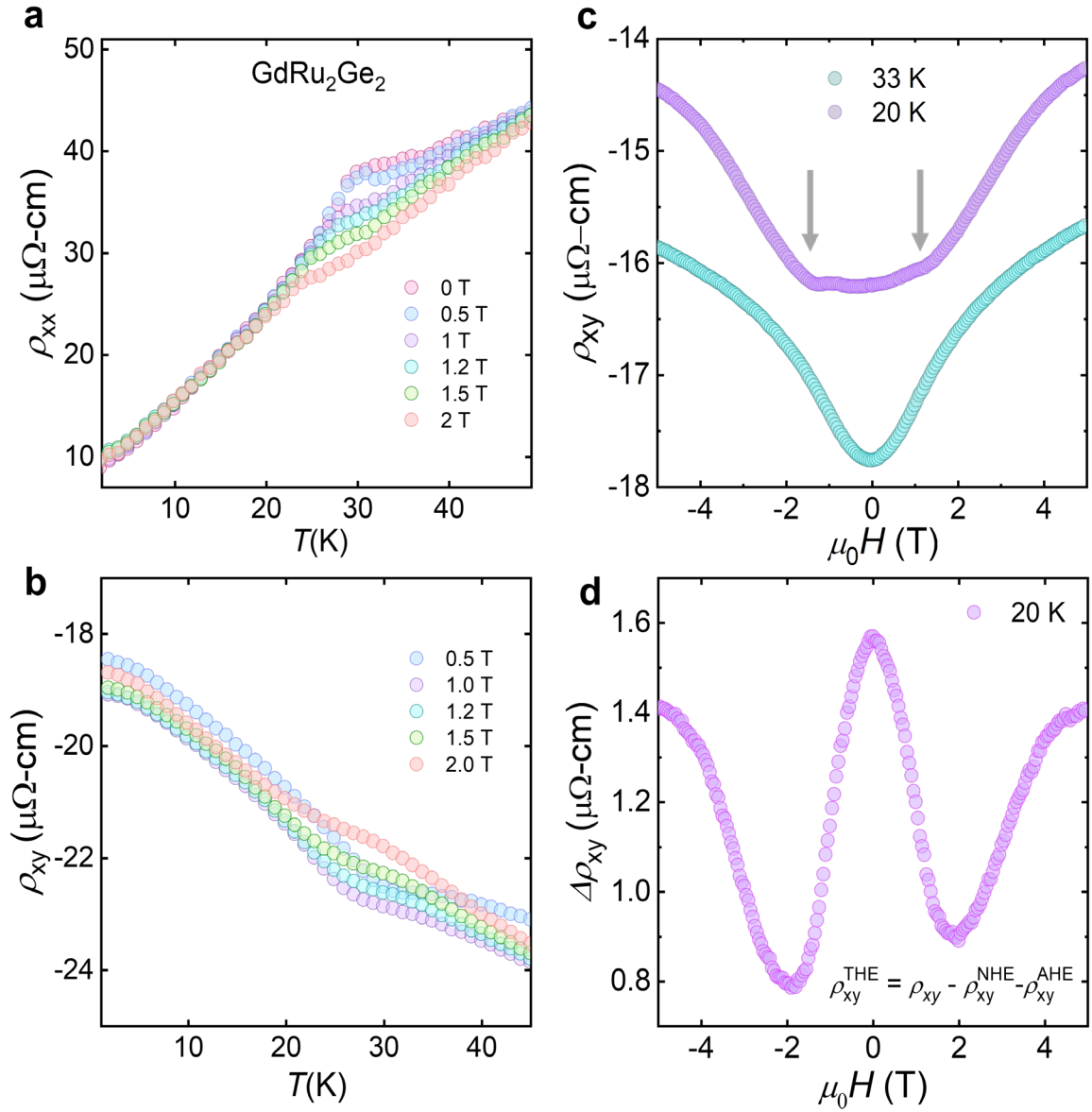


Figure 5. Transport properties of GdRu₂Ge₂ as a function of temperature and magnetic field. **(a)** Longitudinal resistivity (ρ_{xx}) as a function of temperature (T) for different applied magnetic fields (H), **(b)** Transverse (Hall) resistivity (ρ_{xy}) as a function of T for different field values, **(c)** Hall resistivity ρ_{xy} as a function of $\mu_0 H$ at $T = 20$ K and 33 K, showing the evolution of anomalous and topological contributions, and **(d)** Topological Hall resistivity ($\Delta\rho_{xy}$), obtained after subtracting normal and anomalous Hall contributions. The oscillatory behavior suggests a nontrivial magnetic texture.

At $T = 33$ K, ρ_{xy} exhibits a nonlinear feature at different fields (**Figure 5c**), indicating a multiband effect and an anomalous Hall contribution. In contrast, at $T = 20$ K, the field-dependent ρ_{xy} shows two distinct kinks at $\mu_0 H = \pm 1.37$ T (**Figure 5c**), clearly signaling the

presence of topological features. The results of our Hall measurements are consistent with those reported by Yoshimochi et al.^[11]

To estimate THE, we subtracted the Hall resistivity at $T = 20$ K from that at $T = 33$ K. This approach can be justified for the following reasons: (1) the temperature dependence of the ρ_{xy} at a constant field does not show significant variation, and (2) an AFM phase forms at $T = 33$ K, followed by spin reorientation, whereas the skyrmion phase emerges at $T = 20$ K and $\mu_0H = 1.3$ T. At $\mu_0H > 2$ T, the ρ_{xy} data exhibit similar features at $T = 33$ K and 20 K.

The extracted $\Delta\rho_{xy}$ displays a double-peak structure, which is a characteristic feature of topological materials. However, the peak structure is not antisymmetric, as expected for a bulk skyrmion lattice (**Figure 5d**). This discrepancy could be due to carrier scattering being significantly influenced by interfacial effects or domain wall effects, especially when using a pressed pellet.

To get insight into how the electronic structure of GdRu_2X_2 determines their physical properties, pseudopotential spin-polarized density functional theory (DFT) calculations were performed using the Quantum Espresso Software package^[22] employing a projected augmented wave (PAW) method. The results clearly demonstrate some common electronic structure features of the ThCr_2Si_2 structure type (**Figure 6**). The spins of the Gd-4*f* states are polarized, which then polarizes the Ru-4*d*, and X-3*p* states. The contribution of Gd-4*f* states is localized, deep in low energy ~ -8 eV for majority spins and slightly above the Fermi level (E_F) energy ~ 4 eV for minority spins. The spin-polarized band structure and density of states (DOS) of GdRu_2X_2 display a metallic behavior, where multiple bands cross E_F and finite DOS at E_F . Taken together, these features prove that interactions between the localized Gd-4*f* magnetic moments are mediated through the itinerant electrons—RKKY interactions. Comparing the DOS and band structures in **Figure 6**, similar features are represented within the isostructural skyrmion system GdRu_2X_2 (**Figure 6b**). However, the DOS in GdRu_2Si_2 is less diffused than that in GdRu_2Ge_2 due to the different orbital overlaps Si-3*p* vs. Ge-4*p*.

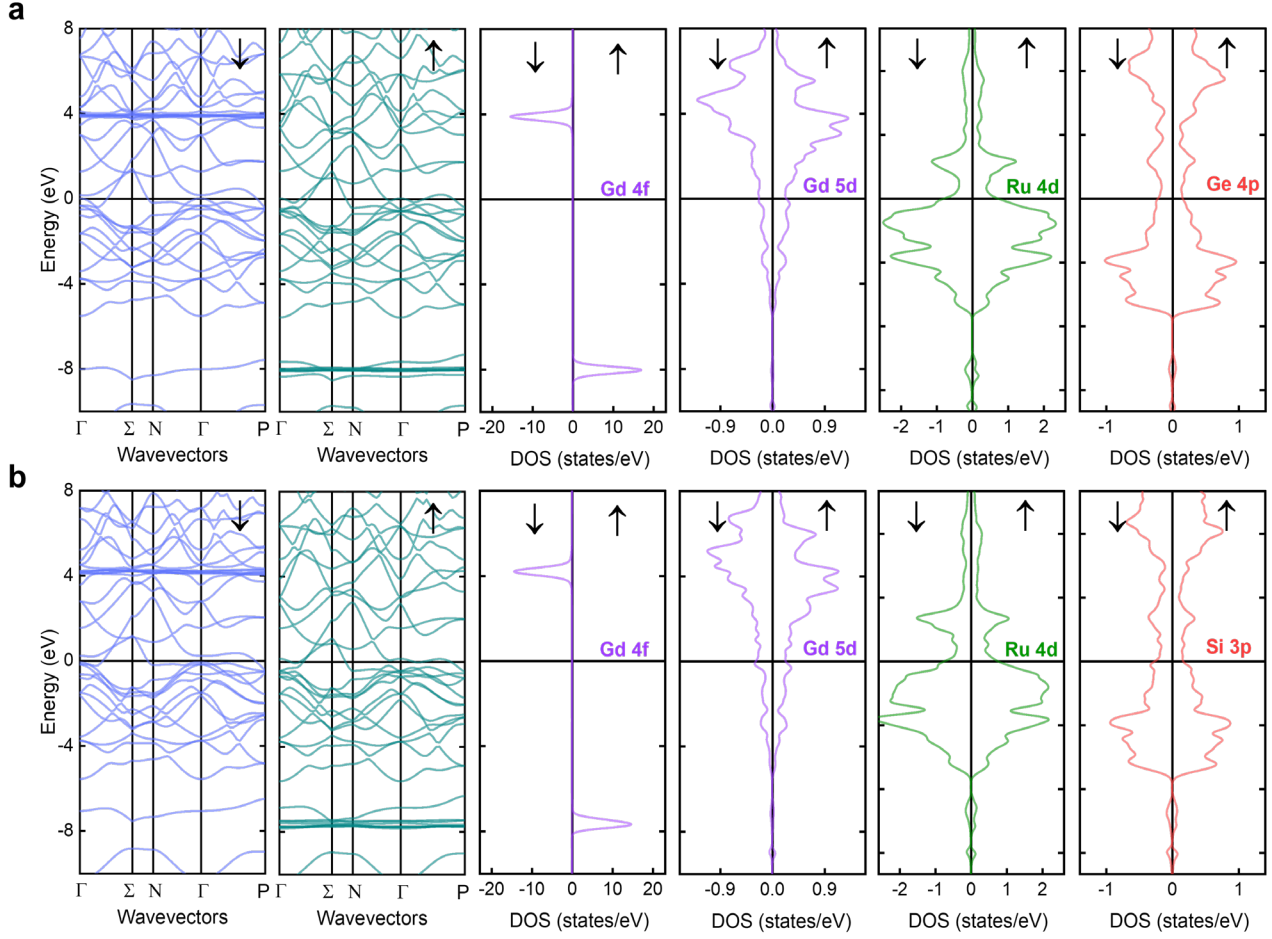


Figure 6. Spin-polarized band structures showing bands around the Fermi level and spin-polarized DOS of **(a)** GdRu₂Ge₂, and **(b)** GdRu₂Si₂.

A quantitative evaluation of the spin exchange interactions was performed for GdRu₂X₂ systems. We performed an energy-mapping analysis using DFT calculations as illustrated in **Figure 7**.^[23] The total energies of the different possible spin configurations were calculated, and these energies were then "mapped" onto the spin Hamiltonian, allowing the spin exchange parameters to be extracted quantitatively. The spin Hamiltonian \hat{H}_{spin} is defined in terms of several different spin exchange parameters as follows:^[23b]

$$\hat{H}_{spin} = -\sum_{i<j} J_{ij} \hat{S}_i \cdot \hat{S}_j \quad (10)$$

where \hat{S}_i and \hat{S}_j are the spins at the sites i and j , and J_{ij} are the spin exchange parameters describing the sign and strength of the interaction between the spin sites i and j . This equation (10) sums up all magnetic interactions within GdRu₂X₂. The Gd spins form two square sublattices within a unit cell. Our model incorporates the nearest-neighbor exchange interaction J_1 along the a - or b -axis, the next nearest-neighbor exchange interaction J_2 within

the ab -plane along the [110] direction, and the interaction J_3 between the Gd square sublattices. To accurately simulate an extended solid and avoid artificial interactions between periodic images of atoms, we used a $(2a, 2b, c)$ supercell (containing four formula units) and six different spin-ordered states (**Figure 7**). The spin-polarized DFT calculations were performed using the Quantum Espresso software package.^[23d] The total spin exchange energy per supercell can be expressed by the following equations:^[24]

$$\begin{aligned}
 E_1 &= E_0 + (-8J_1 + 0J_2 + 0J_3) \cdot S^2 & (11) \\
 E_2 &= E_0 + (0J_1 - 16J_2 + 0J_3) \cdot S^2 \\
 E_3 &= E_0 + (0J_1 + 0J_2 - 8J_3) \cdot S^2 \\
 E_4 &= E_0 + (8J_1 - 8J_2 + 0J_3) \cdot S^2 \\
 E_5 &= E_0 + (8J_1 + 0J_2 + 0J_3) \cdot S^2 \\
 E_6 &= E_0 + (16J_1 - 16J_2 + 0J_3) \cdot S^2
 \end{aligned}$$

where the E_0 corresponds to the non-magnetic contribution to the total energy, and $S = 7/2$, the spin for Gd^{3+} . From these energies, the exchange interactions per four formula units can be calculated as:

$$\begin{aligned}
 J_1 &= \frac{(E_6 - E_2)}{16S^2} & (12) \\
 J_2 &= \frac{(E_5 - E_4)}{8S^2} \\
 J_3 &= \frac{(E_1 + E_5 - 2E_3)}{16S^2}
 \end{aligned}$$

The J -coupling interaction can then be obtained:

Table 1. Calculated J -coupling constants for GdRu_2X_2 ($X = \text{Si}$, and Ge)

X Site	J_1 (K)	J_2 (K)	J_3 (K)
Si	-0.7(2)	-153.5(2)	-0.5(2)
Ge	71.1(2)	-153.8(2)	-2.3(2)

As shown in **Table 1**, J_1 varies from negligible to strong FM when the X site changes from Si

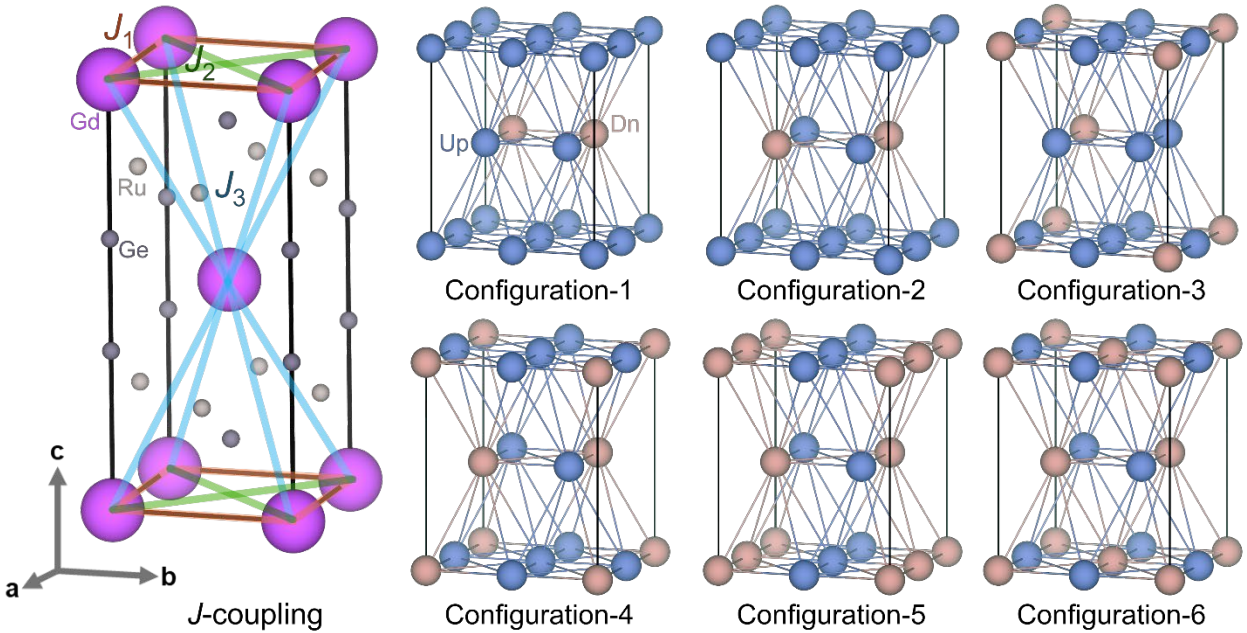


Figure 7. Representing exchange interactions J_1 , J_2 and J_3 between Gd^{3+} atoms within the unit cell and spin-ordered states within the $(2a, 2b, c)$ supercell. Pink and blue colors correspond to the spin up and down, respectively.

to Ge. Meanwhile, stronger AFM interaction J_2 remains unaffected by the X site. Similarly, weak AFM interaction J_3 shows minimal dependence on the X site. This observation aligns well with the magnetic properties of the Si and Ge compounds. Due to the strong in-plane correlations, the spins in the magnetic ground state predominantly align within the ab -plane. Consequently, these in-plane spins are more responsive to magnetic fields applied along the c -axis, resulting in a higher magnetic susceptibility along the c -axis (**Figure 3d**). Our Curie-Weiss analysis and prior work in the literature consistently show a positive Curie-Weiss temperature (θ_{cw}) (**Figure 3c**), suggesting the presence of FM interactions in GdRu_2X_2 .^[16] This competing AFM-FM behavior is illustrated by the upturns and downturns observed in the magnetic susceptibility near the transition temperature, and supported by the hysteresis in the $M(H)$ measurements. The competing FM and AFM interactions in the Gd square lattice (the ab -plane) bear a resemblance to those in other skyrmion hosts.

Taken together, the strong FM interactions (J_1) in GdRu_2Ge_2 lead to more competing AFM-FM exchange interactions in the Ge material compared to the Si sibling. Our results highlight that increased competing exchange interactions at a similar energy scale within the Gd square lattice stabilize multiple topological spin states while making the phase transition to skyrmions more accessible at higher temperatures and lower fields.

CONCLUSIONS

Developing skyrmion materials for spintronics requires the tunability and control of critical temperature and magnetic field conditions at which skyrmions emerge. Our results demonstrate a new, fundamental framework for understanding and realizing rich topological spin phases. We investigated the crystal and electronic structure, magnetic, thermodynamic, and transport properties of the GdRu₂Ge₂ skyrmion material and delved into the impact of competing exchange interactions on the skyrmion evolution in GdRu₂X₂ (X = Si, Ge). GdRu₂Ge₂ displays two skyrmion phases at $0.9 \text{ T} \leq \mu_0 H \leq 1.2 \text{ T}$ and $1.3 \text{ T} \leq \mu_0 H \leq 1.7 \text{ T}$, $2 \text{ K} \leq T \leq 30 \text{ K}$, which are at lower field and higher temperature than that in GdRu₂Si₂ ($2 \text{ T} \leq \mu_0 H \leq 2.5 \text{ T}$, $2 \text{ K} \leq T \leq 20 \text{ K}$).^[8-9] The skyrmions evolution in GdRu₂Ge₂ is proven through magnetization, magnetoentropic mapping, heat capacity, transport and Hall effect measurements. The *J* coupling constants, obtained from our DFT calculations, reveal appreciably stronger FM-AFM competing exchange interactions in GdRu₂Ge₂ compared to GdRu₂Si₂. This is attributable to the more extended Ge-4*p* orbitals than the Si-3*p* orbitals, thus improving the overlap of the atomic interacting wave functions in GdRu₂Ge₂. The enhanced FM-AFM competing interactions in the Ge compound facilitate the phase transition to skyrmions at higher temperatures and lower fields. Further studies are underway to connect chemical bonding and electronic instability to skyrmions evolution. Our work provides a significant step forward for atomically enabled tunability of competing exchange interactions in magnetic metals while linking this insight into the critical conditions at which skyrmions form. This research framework can be applied to develop new skyrmions with designer working conditions for spintronics and logic constructs.

ASSOCIATED CONTENT

Supporting Information. Additional data analysis, tables, figures, including crystallographic data, XRD, SEM-EDS, magnetization, heat capacity, transport measurements TGA, DOS. This material is available free of charge via the Internet at <http://pubs.acs.org>.

AUTHOR INFORMATION

Corresponding Author

*Thao Tran, email: thao@clemson.edu.

Author Contributions

The manuscript was written through contributions of all authors. All authors have given approval to the final version of the manuscript.

Funding Sources

The work at Clemson University was supported by the National Science Foundation under CAREER Award NSF-DMR-2338014. X.H., R.K., and T.T.T thank the Arnold and Mabel Beckman Foundation for a 2023 BYI award to T.T.T. Research performed at Gdansk Tech was supported by the National Science Center (Poland) OPUS grant no. UMO-2022/45/B/ST5/03916. S.T. acknowledges support from ONR-N000142312061.

ACKNOWLEDGMENTS

We thank Dr. C. McMillen, Dr. R. Sachdeva, and Dr. Matthew Powell for their assistance in X-ray diffraction, TGA, and some magnetization, heat capacity measurements, and transport measurements respectively.

References:

- [1] a) A. Fert, N. Reyren, V. Cros, *Nature Reviews Materials* **2017**, 2, 1; b) A. Hirohata, K. Takanashi, *Journal of Physics D: Applied Physics* **2014**, 47, 193001; c) C. Back, V. Cros, H. Ebert, K. Everschor-Sitte, A. Fert, M. Garst, T. Ma, S. Mankovsky, T. L. Monchesky, M. Mostovoy, *Journal of Physics D: Applied Physics* **2020**, 53, 363001; d) C. Psaroudaki, E. Peraticos, C. Panagopoulos, *Applied Physics Letters* **2023**, 123; e) C. H. Marrows, K. Zeissler, *Applied Physics Letters* **2021**, 119; f) K. Wang, W. Wei, H. Du, *Advanced Functional Materials* **2024**, 2416203; g) C. Feng, F. Meng, Y. Wang, J. Jiang, N. Mehmood, Y. Cao, X. Lv, F. Yang, L. Wang, Y. Zhao, *Advanced Functional Materials* **2021**, 31, 2008715.
- [2] a) A. Neubauer, C. Pfleiderer, B. Binz, A. Rosch, R. Ritz, P. G. Niklowitz, P. Böni, *Physical review letters* **2009**, 102, 186602; b) X. Zhang, Y. Zhou, K. M. Song, T.-E. Park, J. Xia, M. Ezawa, X. Liu, W. Zhao, G. Zhao, S. Woo, *Journal of Physics: Condensed Matter* **2020**, 32, 143001; c) Y. Tokura, N. Kanazawa, *Chemical Reviews* **2020**, 121, 2857; d) S. Roychowdhury, P. Yanda, K. Samanta, C. Yi, M. Yao, F. Orlandi, P. Manuel, D. Khalyavin, E. G. D. Valle, P. Constantinou, *Advanced Materials* **2024**, 36, 2305916; e) B. Chen, M. Zeng, K. H. Khoo, D. Das, X. Fong, S. Fukami, S. Li, W. Zhao, S. S. P. Parkin, S. N. Piramanayagam, *Materials Today* **2023**, 70; f) C. Pfleiderer, A. Rosch, *Nature* **2010**, 465, 880; g) J. Jena, S. Koraltan, F. Bruckner, K. Holst, M. Tangi, C. Abert, C. Felser, D. Suess, S. S. P. Parkin, *Advanced Functional Materials* **2024**, 34, 2403358.
- [3] a) X. Huai, T. T. Tran, *Annual Review of Materials Research* **2023**, 53, 253; b) E. E. Oyeka, M. J. Winiarski, A. Błachowski, K. M. Taddei, A. Scheie, T. T. Tran, *Chemistry of Materials* **2021**, 33, 4661; c) N. Kanazawa, S. Seki, Y. Tokura, *Advanced Materials* **2017**, 29, 1603227; d) C. Zhang, Z. Jiang, J. Jiang, W. He, J. Zhang, F. Hu, S. Zhao, D. Yang, Y. Liu, Y. Peng, *Nature Communications* **2024**, 15, 4472; e) Y. Zhang, J. Tang, Y. Wu, M. Shi, X. Xu, S. Wang, M. Tian, H. Du, *Nature Communications* **2024**, 15, 3391; f) D. Singh, Y. Fujishiro, S. Hayami, S. H. Moody, T. Nomoto, P. R. Baral, V. Ukleev, R. Cubitt, N.-J. Steinke, D. J. Gawryluk, *Nature Communications* **2023**, 14, 8050; g) I. Kézsmárki, S. Bordács, P. Milde, E. Neuber, L. M. Eng, J. S. White, H. M. Rønnow, C. D. Dewhurst, M. Mochizuki, K. Yanai, *Nature materials* **2015**, 14, 1116; h) A. Chacon, L. Heinen, M. Halder, A. Bauer, W. Simeth, S. Mühlbauer, H. Berger, M. Garst, A. Rosch, C. Pfleiderer, *Nature physics* **2018**, 14, 936; i) S. Mühlbauer, B. Binz, F. Jonietz, C. Pfleiderer, A. Rosch, A. Neubauer, R. Georgii, P. Böni, *Science* **2009**, 323, 915; j) T. Adams, A. Chacon, M. Wagner, A. Bauer, G. Brandl, B. Pedersen, H. Berger, P. Lemmens, C. Pfleiderer, *Physical review letters* **2012**, 108, 237204; k) T.

- Kurumaji, T. Nakajima, V. Ukleev, A. Feoktystov, T.-h. Arima, K. Kakurai, Y. Tokura, *Physical review letters* **2017**, 119, 237201; l) K. Wang, V. Bheemarasetty, J. Duan, S. Zhou, G. Xiao, *Journal of Magnetism and Magnetic Materials* **2022**, 563, 169905; m) N. Kumar, S. N. Guin, K. Manna, C. Shekhar, C. Felser, *Chemical Reviews* **2020**, 121, 2780; n) S. Parkin, S.-H. Yang, *Nature nanotechnology* **2015**, 10, 195.
- [4] a) D.-H. Kim, M. Haruta, H.-W. Ko, G. Go, H.-J. Park, T. Nishimura, D.-Y. Kim, T. Okuno, Y. Hirata, Y. Futakawa, *Nature materials* **2019**, 18, 685; b) S. Ishiwata, T. Nakajima, J. H. Kim, D. S. Inosov, N. Kanazawa, J. S. White, J. L. Gavilano, R. Georgii, K. M. Seemann, G. Brandl, *Physical Review B* **2020**, 101, 134406; c) T. Kurumaji, T. Nakajima, M. Hirschberger, A. Kikkawa, Y. Yamasaki, H. Sagayama, H. Nakao, Y. Taguchi, T.-h. Arima, Y. Tokura, *Science* **2019**, 365, 914; d) J. M. Moya, S. Lei, E. M. Clements, C. S. Kengle, S. Sun, K. Allen, Q. Li, Y. Y. Peng, A. A. Husain, M. Mitrano, *Physical Review Materials* **2022**, 6, 074201; e) Y. Yasui, C. J. Butler, N. D. Khanh, S. Hayami, T. Nomoto, T. Hanaguri, Y. Motome, R. Arita, T.-h. Arima, Y. Tokura, *Nature communications* **2020**, 11, 5925.
- [5] a) G. Chen, *Nature Physics* **2017**, 13, 112; b) J. Blawat, S. Speer, J. Singleton, W. Xie, R. Jin, *Communications Physics* **2023**, 6, 255.
- [6] a) H. Zhang, X. Y. Zhu, Y. Xu, D. J. Gawryluk, W. Xie, S. L. Ju, M. Shi, T. Shiroka, Q. F. Zhan, E. Pomjakushina, *Journal of Physics: Condensed Matter* **2021**, 34, 034005; b) R. Takagi, N. Matsuyama, V. Ukleev, L. Yu, J. S. White, S. Francoual, J. R. L. Mardegan, S. Hayami, H. Saito, K. Kaneko, *Nature communications* **2022**, 13, 1472; c) T. Nomoto, T. Koretsune, R. Arita, *Physical Review Letters* **2020**, 125, 117204.
- [7] a) S. Hayami, *Journal of Magnetism and Magnetic Materials* **2024**, 604, 172293; b) S. Hayami, Y. Motome, *Physical Review B* **2021**, 103, 024439; c) D. Chakrabartty, M. Sahoo, A. Kumar, S. Jamaluddin, B. Giri, H. Chhabra, K. Pradhan, A. K. Nayak, *ACS nano* **2025**; d) S. Paul, S. Haldar, S. von Malottki, S. Heinze, *Nature communications* **2020**, 11, 4756.
- [8] G. D. A. Wood, D. D. Khalyavin, D. A. Mayoh, J. Bouaziz, A. E. Hall, S. J. R. Holt, F. Orlandi, P. Manuel, S. Blügel, J. B. Staunton, *Physical Review B* **2023**, 107, L180402.
- [9] N. D. Khanh, T. Nakajima, X. Yu, S. Gao, K. Shibata, M. Hirschberger, Y. Yamasaki, H. Sagayama, H. Nakao, L. Peng, *Nature Nanotechnology* **2020**, 15, 444.
- [10] T. Nomoto, R. Arita, *Journal of Applied Physics* **2023**, 133.
- [11] H. Yoshimochi, R. Takagi, J. Ju, N. D. Khanh, H. Saito, H. Sagayama, H. Nakao, S. Itoh, Y. Tokura, T. Arima, *Nature Physics* **2024**, 20, 1.
- [12] J. D. Bocarsly, R. F. Need, R. Seshadri, S. D. Wilson, *Physical Review B* **2018**, 97, 100404.
- [13] J. L. Zuo, D. Kitchaev, E. C. Schueller, J. D. Bocarsly, R. Seshadri, A. Van der Ven, S. D. Wilson, *Physical Review Materials* **2021**, 5, 054410.
- [14] L. Kautzsch, J. D. Bocarsly, C. Felser, S. D. Wilson, R. Seshadri, *Physical Review Materials* **2020**, 4, 024412.
- [15] A. Garnier, D. Gignoux, D. Schmitt, T. Shigeoka, *Physica B: Condensed Matter* **1996**, 222, 80.
- [16] T. Samanta, I. Das, S. Banerjee, *Journal of Applied Physics* **2008**, 104.
- [17] M. Hirschberger, T. Nakajima, S. Gao, L. Peng, A. Kikkawa, T. Kurumaji, M. Kriener, Y. Yamasaki, H. Sagayama, H. Nakao, *Nature communications* **2019**, 10, 5831.
- [18] a) J. A. Blanco, D. Gignoux, D. Schmitt, *Physical Review B* **1991**, 43, 13145; b) D. G. Franco, C. Geibel, *Physical Review B* **2021**, 104, 054416.
- [19] a) E. M. Levin, V. K. Pecharsky, K. A. Gschneidner Jr, G. J. Miller, *Physical Review B* **2001**, 64, 235103; b) H. Hayashi, M. Kato, T. Terashima, N. Kikugawa, H. Sakurai, H. K. Yoshida, K. Yamaura, *Journal of the Physical Society of Japan* **2024**, 93, 094702.

- [20] a) A. Prasad, V. K. Anand, U. B. Paramanik, Z. Hossain, R. Sarkar, N. Oeschler, M. Baenitz, C. Geibel, *Physical Review B—Condensed Matter and Materials Physics* **2012**, 86, 014414; b) D. Ram, J. Singh, S. Banerjee, A. Sundaresan, D. Samal, V. Kanchana, Z. Hossain, *Physical Review B* **2024**, 109, 155152.
- [21] a) S. Li, X. Wang, T. Rasing, *Interdisciplinary Materials* **2023**, 2, 260; b) C. Felser, S. Parkin, *MRS Bulletin* **2022**, 47, 600; c) H. Wang, Y. Dai, G.-M. Chow, J. Chen, *Progress in Materials Science* **2022**, 130, 100971; d) M. Leroux, M. J. Stolt, S. Jin, D. V. Pete, C. Reichhardt, B. Maiorov, *Scientific reports* **2018**, 8, 15510.
- [22] P. Giannozzi, O. Baseggio, P. Bonfà, D. Brunato, R. Car, I. Carnimeo, C. Cavazzoni, S. De Gironcoli, P. Delugas, F. Ferrari Ruffino, *The Journal of chemical physics* **2020**, 152.
- [23] a) M.-H. Whangbo, H.-J. Koo, D. Dai, *Journal of Solid State Chemistry* **2003**, 176, 417; b) H. Xiang, C. Lee, H.-J. Koo, X. Gong, M.-H. Whangbo, *Dalton Transactions* **2013**, 42, 823; c) E. A. Zvereva, G. V. Raganyan, T. M. Vasilchikova, V. B. Nalbandyan, D. A. Gafurov, E. L. Vavilova, K. V. Zakharov, H. J. Koo, V. Y. Pomjakushin, A. E. Susloparova, *Physical Review B* **2020**, 102, 094433; d) P. Giannozzi, S. Baroni, N. Bonini, M. Calandra, R. Car, C. Cavazzoni, D. Ceresoli, G. L. Chiarotti, M. Cococcioni, I. Dabo, *Journal of physics: Condensed matter* **2009**, 21, 395502.
- [24] X. Huai, E. Acheampong, E. Delles, M. J. Winiarski, M. Sorolla, L. Nassar, M. Liang, C. Ramette, H. Ji, A. Scheie, *Advanced Materials* **2024**, 36, 2313763.

Supporting Information For

Atomically Modulating Competing Exchange Interactions in Centrosymmetric Skyrmion Hosts GdRu_2X_2 ($\text{X} = \text{Si}, \text{Ge}$)

Dasuni N. Rathnaweera,¹ Xudong Huai,¹ Ramesh Kumar¹, Michał J. Winiarski,² Tomasz Klimczuk,² and Thao T. Tran^{1,*}

¹Department of Chemistry, Clemson University, Clemson, South Carolina, 29634, United States

²Faculty of Applied Physics and Mathematics and Advanced Materials Center, Gdansk University of Technology, ul. Narutowicza 11/12, 80-233 Gdansk, Poland

Experimental section

List of Figures:

Figure S1. SEM-EDS results of a crystal from Arc-melting

Figure S2. (a) $\chi(T)$ at different magnetic fields $\mu_0 H \perp c$, (b) First derivative of magnetization with respect to temperature, dM/dT for $\mu_0 H \perp c$, (c) A map of $dM/dT = dS/dT$ indicating first-order transitions, for $\mu_0 H \perp c$, (d) First derivative of magnetization with respect to the magnetic field dM/dH curve $\mu_0 H \perp c$, (e) Isothermal magnetic entropy at each different magnetic field obtained by the integral of dM/dT with respect to the magnetic field $\mu_0 H \perp c$.

Figure S3. Temperature-dependent magnetic susceptibility under constant magnetic field (teal) and Curie-Weiss analysis (black) $\mu_0 H \parallel ab$.

Figure S4. Molar heat capacity over temperature (C_p/T) vs. Temperature at different fields, molar heat capacity over temperature (C_p/T) vs. temperature at $\mu_0 H = 0$ and magnetic entropy change from 2 K to 300 K, ΔS_{mag} ($2 \text{ K} \leq T \leq 300 \text{ K}$) fields for powder and crystal sample of GdRu_2Ge_2 .

Figure S5. C_p/T^3 vs. $\log T$ indicating the absence of Einstein mode phonons.

Figure S6. Temperature dependence of magnetoresistance in different fields.

Figure S7. Thermogravimetric analysis of GdRu_2Ge_2

Figure S8: Brillouin zone for body-centered tetragonal lattice.

Figure S9. Pseudopotential spin-polarized decomposed orbital contributions of GdRu_2Ge_2 around the Fermi level.

Figure S10. Pseudopotential non-spin-polarized density of states of GdRu_2Ge_2 around the Fermi level, indicating a larger DOS at Fermi compared to spin-polarized DOS.

List of Tables:

Table S1. Crystal structure information and refinement parameters for GdRu_2Ge_2 obtained by single crystal X-ray diffraction.

Table S2. Fractional Atomic Coordinates and Equivalent Isotropic Displacement Parameters (\AA^2) for GdRu_2Ge_2 . U_{eq} is defined as 1/3 of the trace of the orthogonalised U_{ij} .

Table S3. Bond distances of GdRu_2Ge_2

Table S4. Phonon estimations using two Debye model.

Experimental section

Synthesis.

A sample of GdRu₂Ge₂ was prepared by Arc-melting stoichiometric amounts of constituent elements with a purity > 99.9 wt %. Slight excess Ge was used to compensate for the evaporation during melting. The resultant metal ingot was subjected to subsequent annealing for 5 days under 800 °C in an evacuated quartz tube. Rod-shaped single crystals were mechanically picked from the smashed metal ingot.

Single Crystal X-ray diffraction.

A single metallic black block-shaped crystal of GdRu₂Ge₂ with dimensions 0.12 × 0.10 × 0.06 mm³ was used. It was mounted on a loop with paratone on a Bruker D8 Quest diffractometer. The crystal was kept at a constant $T = 300$ K during data collection. Data were measured using ω scans with Mo K α radiation ($\lambda = 0.71073$ Å) and a Photon 3 detector. Data processing (SAINT) and scaling (SADABS) were performed using the Apex4 software system. The structure was solved by intrinsic phasing (SHELXT) and refined by full-matrix least-squares minimization on F² (SHELXL) using the SHELXTL software program.^[1] All atoms were refined anisotropically.

Powder X-ray diffraction.

Powder X-ray diffraction (PXRD) measurements were performed using Rigaku Ultima IV diffractometer equipped with Cu K α radiation ($\lambda = 1.5406$ Å). Data were collected in the 2θ range of 5–95° at 0.2°/min. Rietveld refinement of the XRD pattern was performed using TOPAS Academic V6.

Magnetization and Specific Heat.

DC magnetization measurements on GdRu₂Ge₂ were performed with the Vibrating sample magnetometer (VSM) option of Quantum Design Physical Properties Measurement System (PPMS) between $2\text{ K} \leq T \leq 300\text{ K}$ at $0\text{ T} \leq \mu_0 H \leq 7\text{ T}$. Heat capacity was measured using the PPMS, employing the semiadiabatic pulse technique from $T = 2$ to 300 K.

Transport measurements.

The electrical and magneto-transport properties (resistivity, magnetoresistance, and Hall effect) were measured in the temperature range of 2–300 K and up to a magnetic field of 5 T using the DC transport option of a Physical Property Measurement System (PPMS, Quantum Design Inc., San Diego) with the conventional four-probe method. Gold leads were attached to the sample using DuPont 4922N silver paint and mixed with butyl acetate for better adhesion. For resistivity and magnetoresistance (MR) measurements, we used a bar-shaped sample with dimensions $2 \times 0.6 \times 0.5$ mm³, while a pressed pellet with dimensions $3 \times 3 \times 0.15$ mm³ was used for Hall effect measurements. This approach was chosen to satisfy the $w \gg t$ geometry required for observing an appreciable Hall signal, as the aspect ratio $w/t \approx 20$ is more suitable for Hall measurements in polycrystalline samples.

Thermogravimetric analysis.

Thermogravimetric analysis and differential scanning calorimetry measurements were performed using a TA SDTQ600 Instrument. Approximately 15 mg of GdRu₂Ge₂ powder was placed in an alumina crucible and heated at a rate of 20 °C/min from room temperature to 1000 °C under flowing nitrogen of flow rate: 100mL/min; Figure S1).

Scanning electron microscopy analysis.

SEM-EDS analysis was conducted using a Hitachi SU5000 VP-SEM equipped with a Schottky Field Emission source for imaging. An Oxford EDS system was utilized to verify the Gd:Ru:Ge ratio, and the data was processed using AZtecLive software.

Density Functional theory calculations.

Pseudopotential band structure and polarized density of states were calculated using the pw.x program in the Quantum Espresso (QE) software package,^[2] with the Generalized Gradient Approximation of the exchange-correlation potential and Hubbard U correction (GGA+U) for the strong correlations in 4*f* bands (6.7 eV for Gd-4*f*)^[3] of the exchange-correlation potential with the PBEsol parametrization.^[4] Projector-augmented wave (PAW) potentials for Ge, and Ru were taken from the PSlibrary v.1.0.0 set, and for Gd, PAW potential developed by VLab was used.^[5] The self-consistencies were carried out using $13 \times 13 \times 6$ *k*-mesh in the irreducible Brillouin zone. Kinetic energy cutoff for charge density and wavefunctions was set to 60 eV and 412 eV. The pseudo potential DFT calculations for the *J*-coupling constant used the same parameter, except the *k*-mesh was changed to $3 \times 3 \times 2$ to account for the (2a×2b×c) super cell.

Figure S1. SEM-EDS results of a GdRu_2Ge_2 crystal from arc-melting, showing the agreement between the experimental Gd:Ru:Ge ratio of 1:2:2 and the theoretical ratio of 1:2:2.

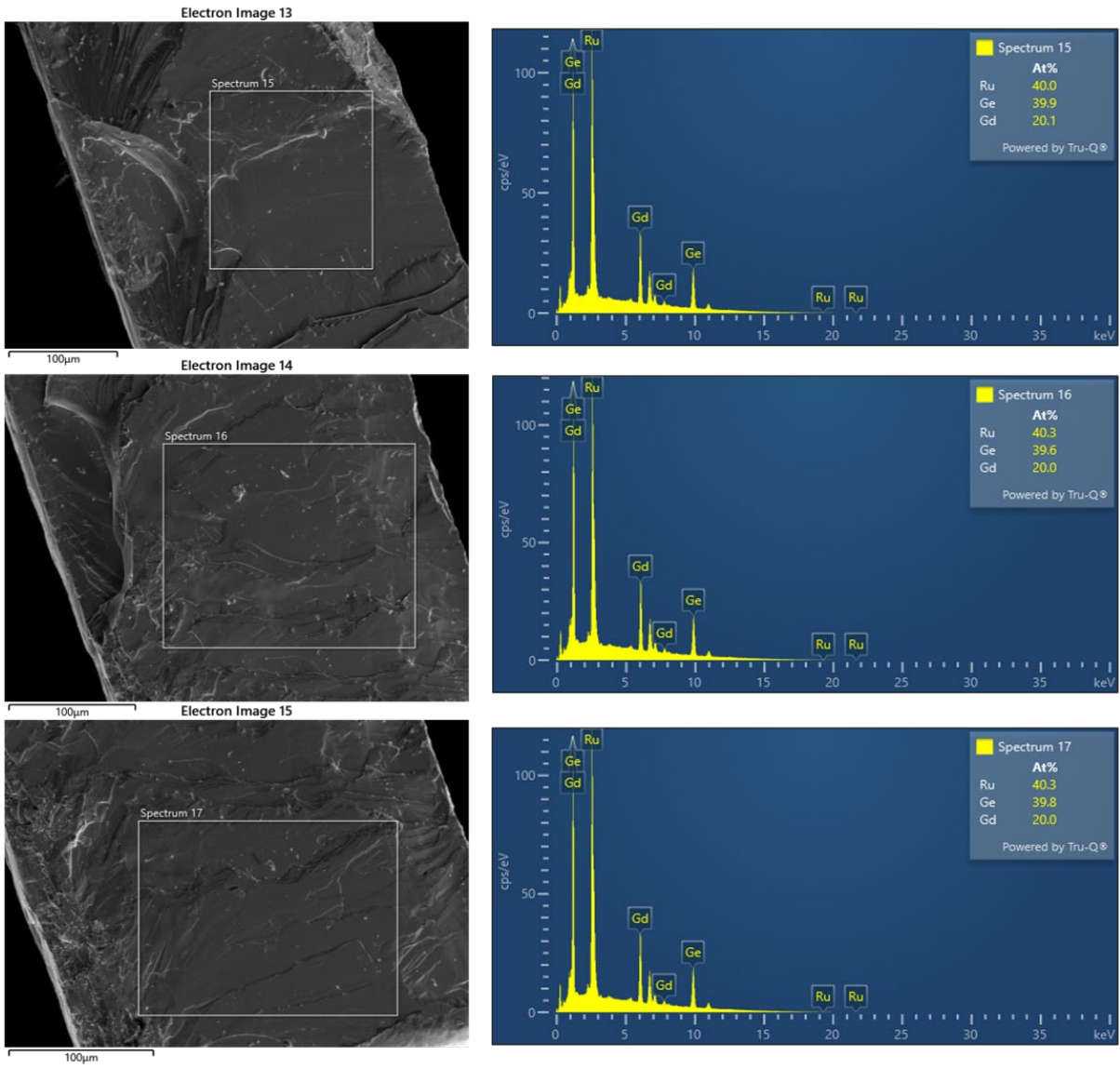


Figure S2. (a) $\chi(T)$ at different magnetic fields $\mu_0 H \perp c$, (b) First derivative of magnetization with respect to temperature, dM/dT for $\mu_0 H \perp c$, (c) A map of $dM/dT = dS/dT$ indicating first-order transitions, for $\mu_0 H \perp c$, (d) First derivative of magnetization with respect to the magnetic field dM/dH curve $\mu_0 H \perp c$, (e) Isothermal magnetic entropy at each different magnetic field obtained by the integral of dM/dT with respect to the magnetic field $\mu_0 H \perp c$.

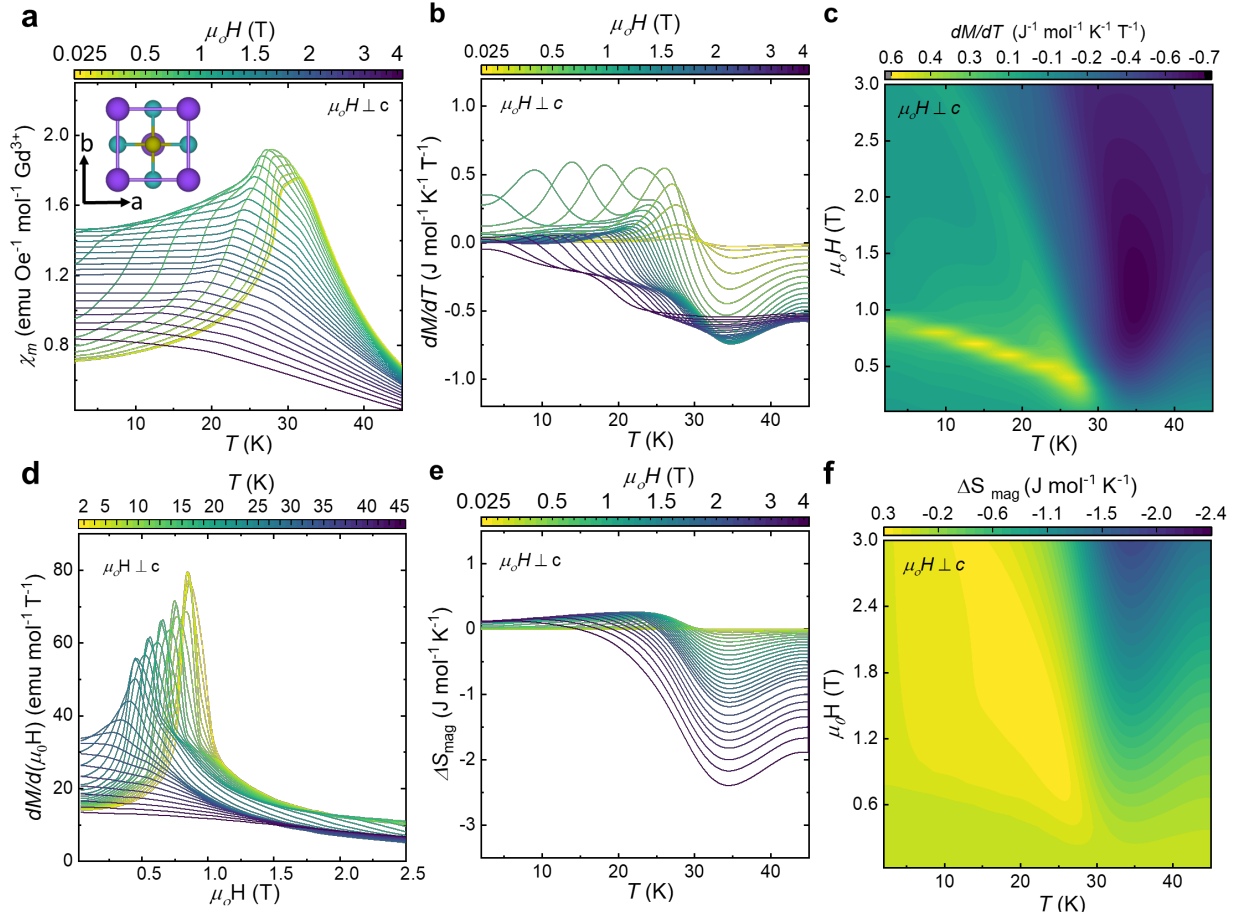


Figure S3. Temperature-dependent magnetic susceptibility under constant magnetic field (teal) and Curie-Weiss analysis (black) $\mu_0 H \parallel ab$.

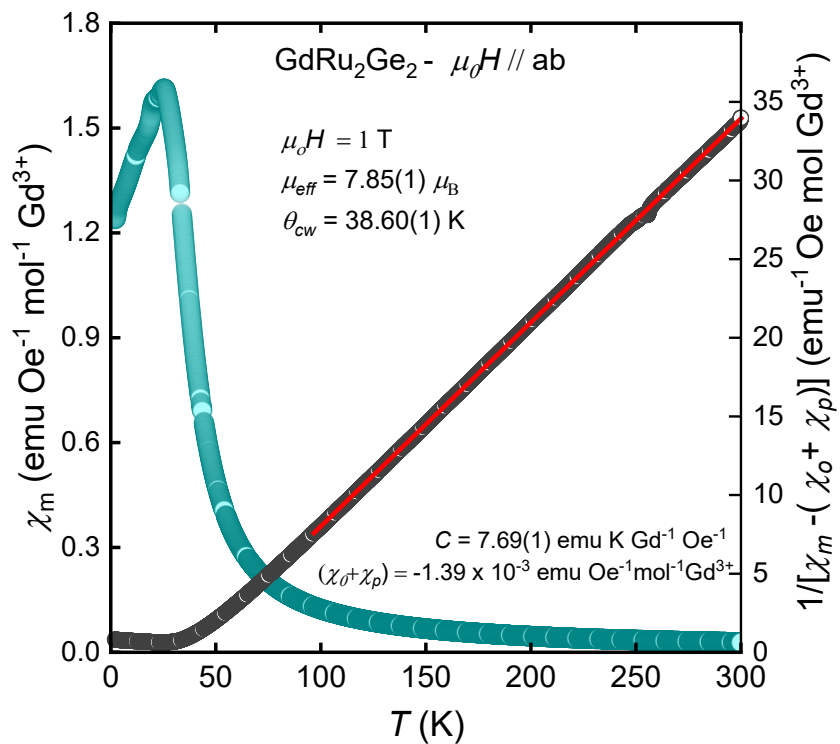


Figure S4. (a) Molar heat capacity over temperature (C_p/T) vs. Temperature at different fields for powder sample, (b) Molar heat capacity over temperature (C_p/T) vs. temperature at $\mu_0 H = 0$ for GdRu₂Ge₂ powder, and magnetic entropy change from 2 K to 300 K, ΔS_{mag} ($2 \text{ K} \leq T \leq 300 \text{ K}$) = 8.5(1) J mol f.u.⁻¹ K⁻¹ (purple line), expected value for Rln(8) (red line).

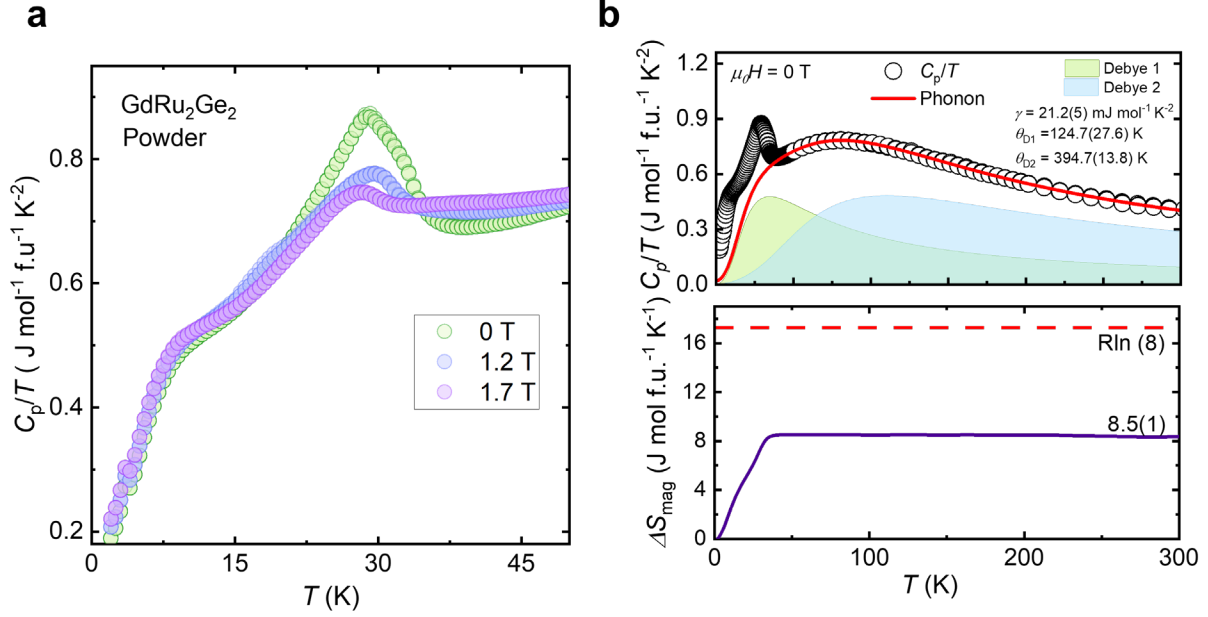


Figure S5. C_p/T^3 vs $\log T$ at zero field indicating the absence of Einstein mode phonons.

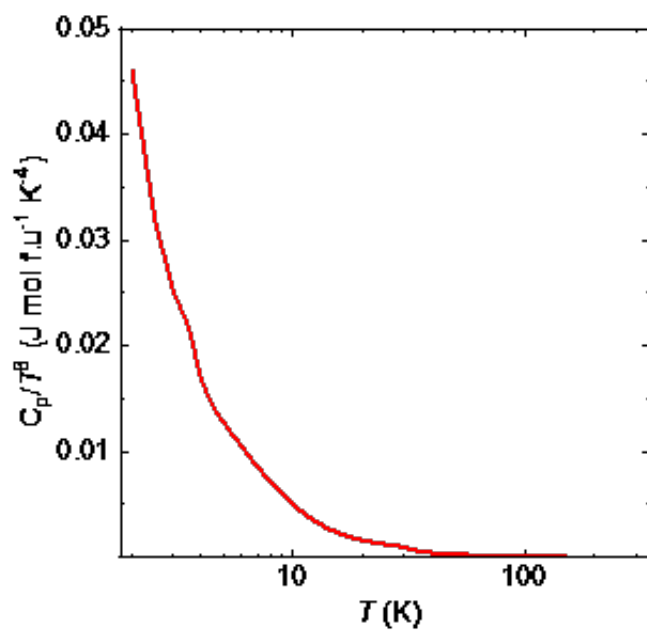


Figure S6. Temperature dependence of magnetoresistance in different fields.

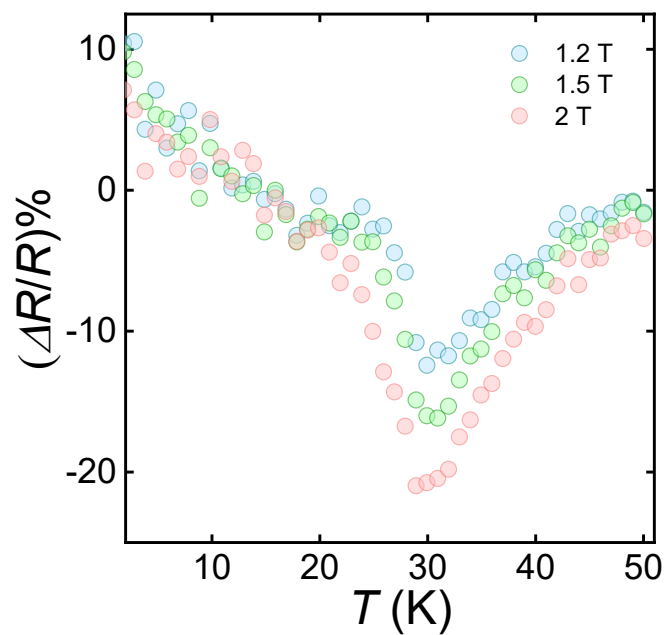


Figure S7. Thermogravimetric analysis of GdRu_2Ge_2 indicating the congruent melting nature.

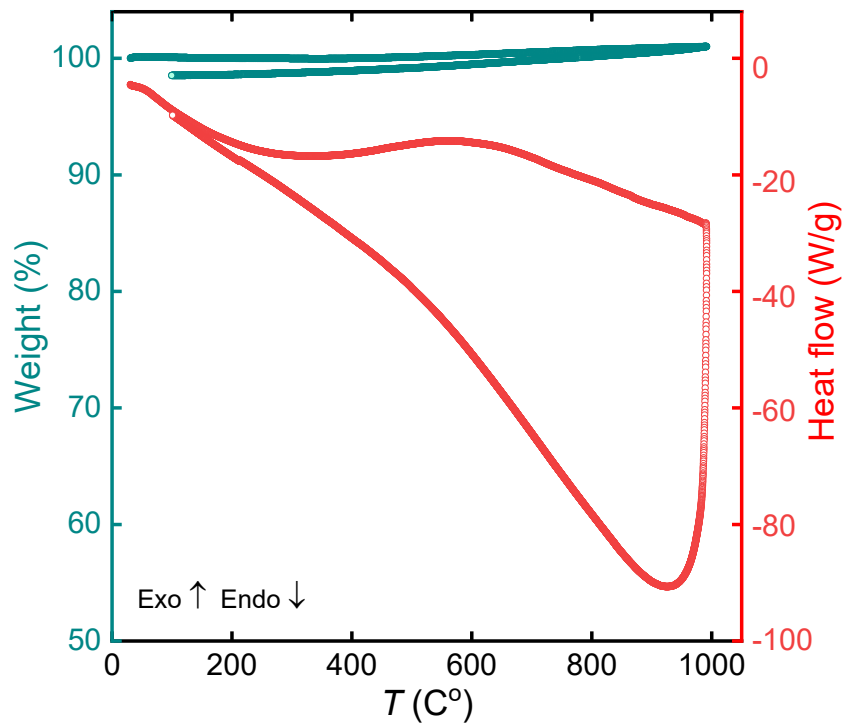


Figure S8. Brillouin zone for body-centered tetragonal lattice.^[5b, 6]

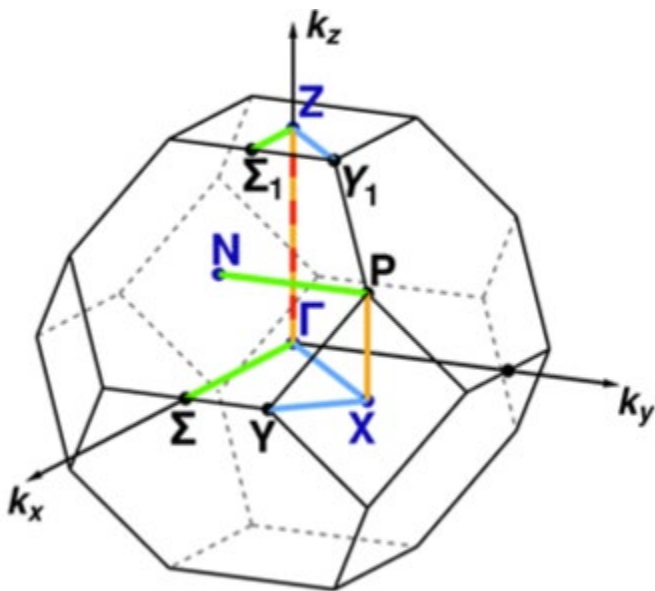


Figure S9. Pseudopotential spin-polarized decomposed orbital contributions of GdRu₂Ge₂ around the Fermi level.

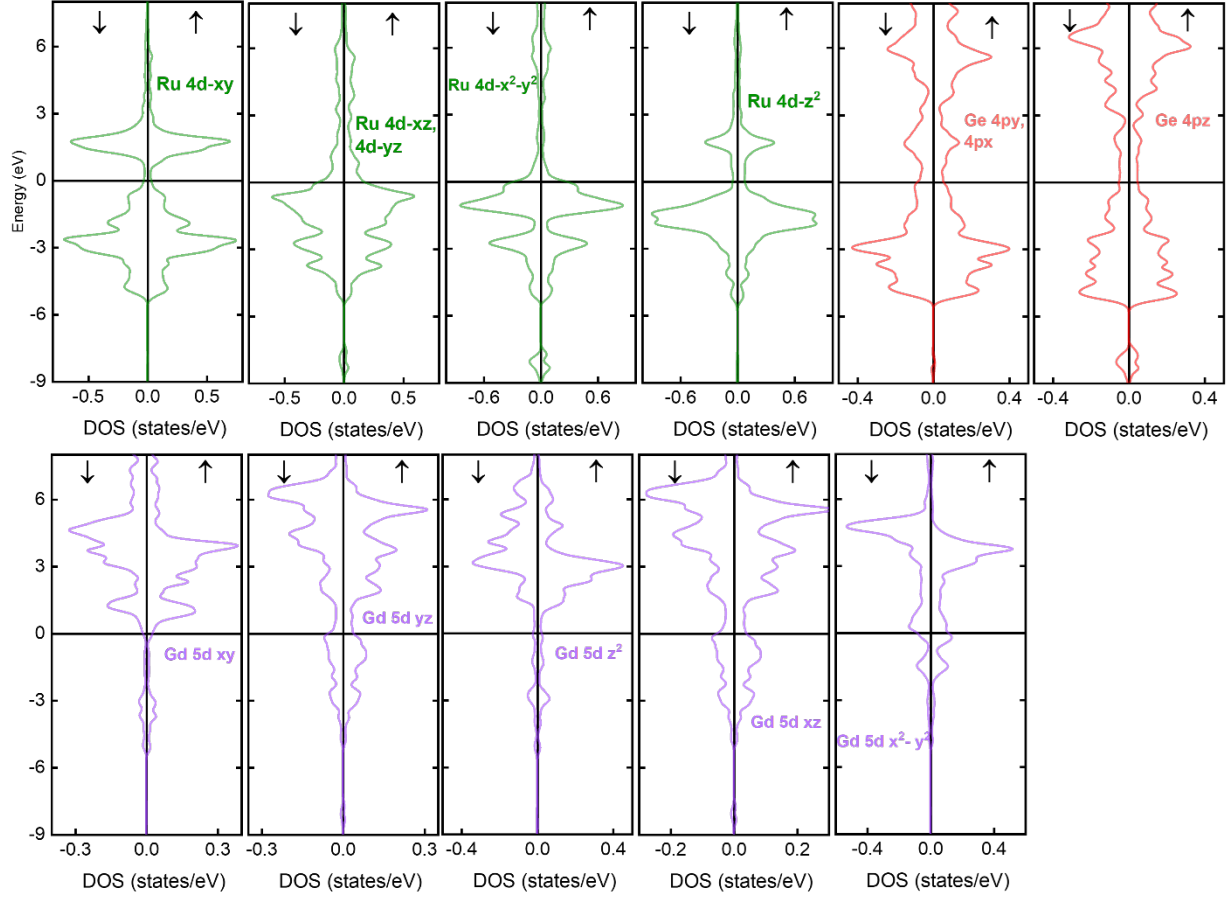
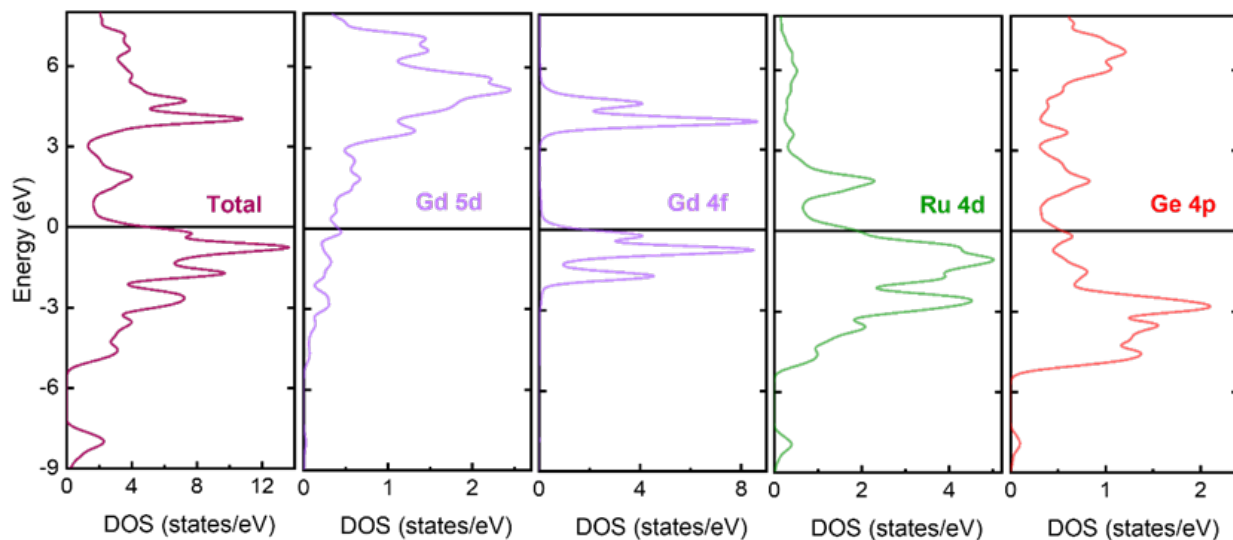


Figure S10. Pseudopotential non-spin-polarized density of states of GdRu_2Ge_2



The DFT results without spin-polarization reveal diffuse Gd-4*f* orbital near the Fermi level, which is inconsistent with the localized nature of the 4*f* states, confirming the magnetic properties of the material.

Table S1. Crystal structure information and refinement parameters for Gd obtained by single crystal X-ray diffraction.

Formula	GdRu ₂ Ge ₂
$D_{\text{calc.}}/\text{g cm}^{-3}$	9.486
m/mm^{-1}	43.344
Formula Weight	504.608
T/K	300(2)
Crystal System	tetragonal
Space Group	$I4/mmm$
$a/\text{\AA}$	4.2316(1)
$b/\text{\AA}$	4.2316(1)
$c/\text{\AA}$	9.8797(5)
$V/\text{\AA}^3$	176.91(1)
Z	2
Wavelength/ \AA	0.71073
Radiation type	Mo K_{α}
$\theta_{\text{min}}/^\circ$	5.242
$\theta_{\text{max}}/^\circ$	29.516
Goof	1.235
wR_2	0.0323
R_1	0.0134

Table S2. Fractional Atomic Coordinates and Equivalent Isotropic Displacement Parameters (\AA^2) for GdRu₂Ge₂. U_{eq} is defined as 1/3 of the trace of the orthogonalised U_{ij} .

Atom	x	y	z	U_{eq}
Gd1	1.500000	0.500000	0.500000	0.0075(2)
Ru1	1.000000	0.500000	0.250000	0.0053(2)
Ge1	0.500000	0.500000	0.13007(8)	0.0060(2)

Table S3. Bond distances of GdRu₂Ge₂

Bond type	Bond distance (Å)
Gd - Gd	4.2316(1)
Ru-Ru	2.9922(1)
Ge-Ge	2.5701(9)
Gd - Ru	3.2523(1)
Gd-Ge	3.2565(4)
Ru-Ge	2.4250(4)

Table S4a. Phonon estimation using two Debye models (crystal sample)

Variable	Fitted value
Number of oscillators in Debye-1 mode	3 (Fixed)
Number of oscillators in Debye-2 mode	2 (Fixed)
Debye temperature 1	457.2 (2.2) K
Debye temperature 2	175.8 (1.4) K
γ	9.6 (1) mJ mol ⁻¹ K ⁻²
R ²	0.99854

Table S4b. Phonon estimation using two Debye models (powder sample)

Variable	Fitted value
Number of oscillators in Debye-1 mode	1.2(2)
Number of oscillators in Debye-2 mode	3.7(2)
Debye temperature 1	123.4(27.6) K
Debye temperature 2	394.7(13.8) K
γ	21.21(5.1) mJ mol ⁻¹ K ⁻²
R ²	0.99953

References:

- [1] G. M. Sheldrick, *Acta Crystallographica Section C: Structural Chemistry* **2015**, 71, 3.
- [2] P. Giannozzi, O. Basergio, P. Bonfà, D. Brunato, R. Car, I. Carnimeo, C. Cavazzoni, S. De Gironcoli, P. Delugas, F. Ferrari Ruffino, *The Journal of chemical physics* **2020**, 152.
- [3] L. Wang, T. Maxisch, G. Ceder, *Physical Review B* **2006**, 73, 195107.
- [4] J. P. Perdew, A. Ruzsinszky, G. I. Csonka, O. A. Vydrov, G. E. Scuseria, L. A. Constantin, X. Zhou, K. Burke, *Physical review letters* **2008**, 100, 136406.
- [5] a) M. Topsakal, R. M. Wentzcovitch, *Computational Materials Science* **2014**, 95, 263; b) P. Giannozzi, S. Baroni, N. Bonini, M. Calandra, R. Car, C. Cavazzoni, D. Ceresoli, G. L. Chiarotti, M. Cococcioni, I. Dabo, *Journal of physics: Condensed matter* **2009**, 21, 395502.
- [6] M. M. Hirschmann, A. Leonhardt, B. Kilic, D. H. Fabini, A. P. Schnyder, *Physical Review Materials* **2021**, 5, 054202.